PHYSICAL REVIEW C VOLUME 56, NUMBER 1 JULY 1997

ARTICLES

Kinematically complete measurement of $pp \rightarrow pn\pi^+$ near threshold

J. G. Hardie,* S. A. Dytman, W. W. Daehnick, W. K. Brooks,† and R. W. Flammang
Department of Physics and Astronomy, University of Pittsburgh, Pittsburgh, Pennsylvania 15260

L. C. Bland, W. W. Jacobs, P. V. Pancella,‡ and T. Rinckel
Indiana University Cyclotron Facility, Bloomington, Indiana 47408

J. D. Brown and E. Jacobsen
Physics Department, Princeton University, Princeton, New Jersey 08540

(Received 6 September 1996)

Cross sections for $pp \rightarrow pn\pi^+$ have been measured at incident proton energies of 294.3, 299.3, 306.3, 314.1, and 319.2 MeV ($0.11 < \eta < 0.42$) to investigate hadronic π^+ production near threshold. Pion angular distributions are presented for 294.3, 299.3, and 319.2 MeV. At 294.3 and 299.3 MeV they are consistent with isotropy, indicating s-wave dominance for the angular momentum of the $\pi^+ pn$ system. The shapes of the pn, $n\pi^+$, and $p\pi^+$ invariant mass distributions provide further evidence for dominance of s-wave mechanisms close to threshold. At 319.2 MeV significant anisotropy indicates contributions from higher partial waves. The total cross sections show an energy dependence consistent with an early partial conservation of axial current based calculation and with a recent calculation that considers only s-wave contributions. Tentative values for the strongest contributing partial wave amplitudes are presented. [S0556-2813(97)01307-1]

PACS number(s): 25.10.+s, 11.40.Ha, 13.75.Cs, 21.30.Cb

I. INTRODUCTION

The study of pion production processes close to threshold originally was initiated in order to explore the application of fundamental symmetries to near-threshold phenomena. Current algebra and soft pion techniques [1] were utilized, and isospin symmetry and general commutation relationships between operators were exploited. A central hypothesis in these investigations was the partial conservation of axial current (PCAC), where the pion current is taken as the primary mediator for low energy processes such as pion decay, Gamov-Teller neutron decay, and pion-nucleon scattering. The relations derived from these considerations are called the low energy theorems, and modern models often use them as their starting point. Chiral perturbation theory [2] has recast these ideas in modern language and has put them on a firmer theoretical basis. Experimental capabilities have now developed to the point where these ideas can be tested in detail. So far the primary application in nuclear physics has been to near-threshold photoproduction of π^0 mesons from the proton. The leading order chiral perturbation theory calculations [3] are in good agreement with the π^0 cross section data from Bonn [4].

The major subject of this paper is an experimental study of $pp \rightarrow pn\pi^+$ very close to threshold. Gell-Mann and Watson [5] and Rosenfeld [6] examined the properties of pion production through pp as well as γp collisions near threshold, including the $pp \rightarrow pn\pi^+$ reaction. They used general isospin and phase space arguments to predict the spin, isospin, and energy dependence of the cross section and introduced much of the terminology for pp inelastic reactions in use today. Schillaci, Silbar, and Young [7] used these ideas to calculate the energy dependence of the total cross sections of all pp inelastic channels near threshold. They used PCAC for the pion vertex, the Adler-Dothan theorem [8] to simplify the calculation, and fitted NN phase shifts.

Modern hadron facilities such as the Indiana University Cyclotron Facility (IUCF) have the capability for much improved accuracy in pion production experiments very close to threshold. The first results from the Indiana Cooler ring were published by Meyer *et al.* [9] for the total cross sections of $pp \rightarrow pp\pi^0$. The lowest beam energy used was 5.4 MeV above π^0 threshold, where the maximum pion energy in the center-of-mass (c.m.) frame was 2.3 MeV. Since the thresholds differ for various hadronic pion production processes, it is convenient to present results in terms of η, the maximum pion momentum in the c.m. frame measured in units of the pion mass. In this notation the data of Ref. [9] closest to threshold have $\eta = 0.186$. Recent results from CELSIUS (Uppsala) [10] for the same interaction are in excellent agreement with the data of Meyer *et al.*, and with η as low as 0.08 extend the $pp \rightarrow pp\pi^0$ data even closer to threshold (the maximum pion kinetic energy in the c.m. frame at their lowest energy is 0.40 MeV). Older total cross section mea-

---

*Present address: Department of Physics and Computer Science, Christopher Newport University, Newport News, Virginia 23601.

†Present address: Thomas Jefferson National Accelerator Facility, Newport News, Virginia 23606.

‡Present address: Physics Department, Western Michigan University, Kalamazoo, Michigan 49007.

surements for $pp\rightarrow pp\pi^0$ from TRIUMF [11] are of lower accuracy, but in agreement with the more recent results. TRIUMF results of differential cross sections and analyzing powers for $pp\rightarrow d\pi^+$ have been published by Korkmaz *et al.* [12] and of total cross sections for $np\rightarrow d\pi^0$ by Hutcheon *et al.* [13]. The lowest energy $np\rightarrow d\pi^0$ data have $\eta=0.015$. The first experimental cross sections for $pp\rightarrow pn\pi^+$ near threshold (with a minimum η of 0.112) were reported in a recent Letter by the present authors [14]. The pion angular distributions were shown to be close to isotropic, indicating sensitivity to the s wave. This paper provides a more complete analysis of the same data set.

A major interest in experiments near threshold is the possibility to learn about the πNN vertex. Within a few MeV of threshold, the s wave will dominate unless there is a nearby resonance. Experiments at intermediate energy facilities have previously studied the role of the P_{33} πN resonance (the Δ) that peaks at 1232 MeV πN c.m. energy and has a width of 120 MeV. Experiments at total πN c.m. energies well below the Δ mass are required to deduce the strength of the πN s wave and compare it with theoretical predictions. In conjunction with a calculation that focused on the effects of the Δ intermediate state, Lee predicted that the Δ contribution to $pp\rightarrow pn\pi^+$ (which can enter through either the NN or πN interaction) is roughly 15% of the total cross section [15]. Similarly, a recent calculation of Engel *et al.* suggests that the contribution of a delta isobar is not important at energies below 350 MeV [16].

Current determinations of the on-shell πNN coupling strength by low energy NN and πN scattering experiments agree to within about 5%, but the off-shell dependence is much less certain and has proved to be quite model dependent. The off-shell πNN interaction is masked in most experiments by the strength of the Δ resonance. It is often parametrized in terms of a vertex range (also referred to as a cutoff momentum) in a monopole form factor with published results in the range of 0.6–1.5 GeV/c. Determinations based on πN data [17,18] tend towards the low end of that interval, and fits to NN data give the higher values [19,20]. The fit to $pp\rightarrow d\pi^+$ by Vogelzang, Bakker, and Boersma [21] also requires a vertex range below 0.9 GeV.

The diagrams expected to contribute most strongly to $NN\rightarrow NN\pi$ reaction close to threshold are shown in Fig. 1. Since the pion momentum must be provided by two nucleons, direct production from a single nucleon [Fig. 1(a)] would normally be a minor contributor in $NN\rightarrow NN\pi$ reactions. A more likely contribution comes from the rescattering diagram shown in Fig. 1(b). Close to threshold the exchanged particle should be the pion because of its low mass, but the contribution of other mesons [Fig. 1(c)] and the Δ resonance [Fig. 1(d)] in the intermediate state must be considered. All of the diagrams in Fig. 1 depend on the s-wave πNN strength. Intermediate state particles are off shell, and their momentum is not fixed even when the external kinematics are fixed.

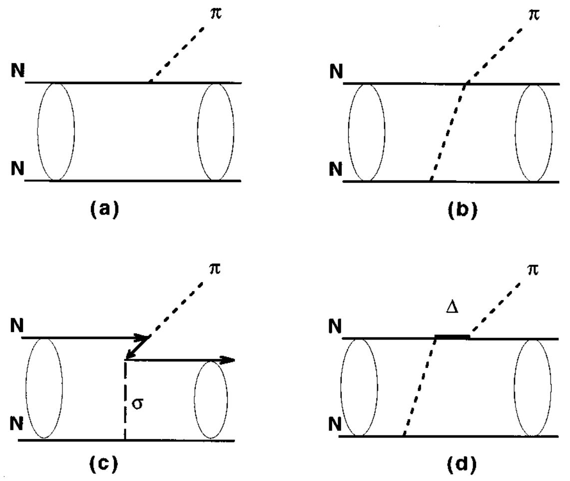

FIG. 1. Diagrams showing the most basic processes contributing to the $NN\rightarrow NN\pi$ reactions. Diagram (a) signifies direct production, (b) indicates pion rescattering, (c) involves heavy meson exchange, and (d) is production through the Δ resonance.

Evidence for s-wave dominance in the hadronic pion production processes is mixed. For the $pp\rightarrow d\pi^+$ reaction, the analyzing power seen by Korkmaz *et al.* [12] is significant even at the lowest beam energy, 3.2 MeV above threshold. This implies a strong p-wave (or higher angular momentum) πN strength independent of any model. On the other hand, dominance of the s-wave πN reaction for the $pp\rightarrow pp\pi^0$ data seemed established based on the observation that the energy dependence follows the phase space for a reaction mechanism with s waves in both the NN and πN interactions [9]. However, the magnitude of the cross section was not explained by calculations based on the traditional approach of Koltun and Reitan or Miller and Sauer [22,23], where only pion-mediated interactions were included and evaluated on shell. The total cross sections obtained in these calculations were a factor of about 5 smaller than the experimental results. The simplest diagrams are insufficient even if carefully calculated using modern NN potentials. Part of the explanation is that the leading pion rescattering diagram is suppressed for π^0 production because the isospin independent πN scattering length (often parametrized as λ_1) is unusually small.

Schillacci, Silbar, and Young [7] used on-shell s-wave πNN information and had to estimate the off-shell $NN\rightarrow NN$ interaction in the intermediate state, which led to an estimated uncertainty of a factor of 2, a range that did include the new IUCF $pp\rightarrow pp\pi^0$ cross sections [9]. Subsequent calculations by Lee and Riska [24] and Horowitz, Meyer, and Griegel [25] are similar in spirit although the NN scattering diagrams are explicitly calculated. All of these authors use only s-wave pion production. The last two calculations add reaction mechanisms involving isoscalar heavy mesons in the intermediate state [Fig. 1(c) with a σ or ω].

The discussion about the appropriate treatment for $pp\rightarrow pp\pi^0$ is continuing. A different explanation for the underprediction has been advanced by Hernandez and Oset [26] who generate a large off-shell pion rescattering contribution. A recent paper by Hanhart *et al.* [27] reexamines the assumptions of the above formulations by treating the hadron kinematics exactly and by including all terms in the pion production Hamiltonian. It is of interest that their result for direct pion production [Fig. 1(a)] has a smaller magnitude (factor of roughly 2) than the earlier calculations [9,23,22] and a somewhat different energy dependence. With a different formalism than Hernandez and Oset they also find a much smaller enhancement due to the off-shell effects in pion rescattering. Finally, two calculations using a heavy baryon formulation of chiral perturbation theory have been published [28,29] for $pp\rightarrow pp\pi^0$. They evaluate the direct diagram, pion rescattering, and the lowest order Δ diagram, and obtain total cross sections a factor of about 5 lower than experiment [9].

In 1996 Engel *et al.* [16] published a relativistically covariant one-boson-exchange calculation that presents cross sections for $pp\rightarrow pp\pi^0$ as well as $pp\rightarrow pn\pi^+$ for the energy range of 300 MeV to 2 GeV. The neglect of final state interactions in the published study significantly diminishes their expected accuracy near threshold. However, a recent report by Shyam and Mosel [16] rectifies this omission and obtains cross sections within about 25% of the $pp\rightarrow pn\pi^+$ cross sections presented below, as well as of the available $pp\rightarrow pp\pi^0$ data.

Previous to this experiment, the lowest beam energy for which modern cross sections were published was 400 MeV [30], compared to a threshold energy of 292.3 MeV. For earlier data closer to threshold, the separation of $pp\rightarrow pn\pi^+$ from $pp\rightarrow d\pi^+$ was difficult and ambiguous. Thus, s-wave dominance had not been established for $pp\rightarrow pn\pi^+$. The present experiment was designed to measure the angular distributions for $pp\rightarrow pn\pi^+$ to address this issue [14]. The experimental difficulties in pp threshold experiments are considerable. Unless an essentially pure or windowless hydrogen target is used, pion production from target impurities or the target windows will dominate. In this experiment one must measure a small cross section, of order 1 μb, by either detecting very low energy pions or reaction nucleons that are confined to very small laboratory angles. The Indiana Cooler Ring provided a suitable site for this type of work. The standard internal target is a reliable, windowless hydrogen jet of adequate density (up to 10^{16} atoms/cm^2), and beam improvements in recent years have led to a very low level of background. In addition, a large-aperture 6° bending magnet was designed and installed for this experiment and has become a permanent part of the ring. As a consequence the detection of reaction protons and neutrons at very small angles became practical, and kinematically complete measurements could be made for the energies of interest.

In this paper, we present and discuss differential cross sections for the reaction $pp\rightarrow pn\pi^+$ near threshold. Beam energies from 294.3 MeV (2 MeV over threshold) to 319.2 MeV were used. At the lowest energy, the maximum pion c.m. kinetic energy is 0.86 MeV. By completely determining the final state momenta, we can calculate the cross section with respect to any variable. A more detailed, unpublished account of the analysis methods is available [31]. Since a novel experimental technique was employed, we present details of the experiment and a discussion of the normalization and acceptance issues. Cross sections will be presented with respect to beam energy, the π angle in the c.m. frame, and the pn, $p\pi^+$, and $n\pi^+$ invariant masses.

II. EXPERIMENTAL CONSIDERATIONS

A. Kinematics

The threshold for the reaction $pp\rightarrow pn\pi^+$ is 292.3 MeV. Very close to threshold, the reaction products have negligible kinetic energy in the center-of-mass frame. This means that all three reaction products emerge near 0° in the laboratory frame. For energies above the pion production threshold, kinematics give the maximum laboratory frame scattering angle θ_i of the ith particle as

TABLE I. Kinematic limits of the laboratory polar angles for the outgoing particles in the reaction $pp\rightarrow pn\pi^+$.

Beam energy (MeV)	$\theta^p_{\max}\simeq\theta^n_{\max}$ (deg)	$\theta^\pi_{\max}$ (deg)
294.3	4.75	16.5
299.3	8.8	31.7
306.3	12.3	47.4
314.1	15.2	65.7
319.2	16.8	180.0

$$\tan\theta_i=\frac{\beta_i}{\gamma_{\text{c.m.}}\beta_{\text{c.m.}}\sqrt{1-\beta_i^2/\beta_{\text{c.m.}}^2}}, \tag{1}$$

where $\gamma_{\text{c.m.}}$ and $\beta_{\text{c.m.}}$ are the usual relativistic kinematic parameters of the center-of-mass frame relative to the laboratory frame. β_i is the maximum velocity of the ith particle in the center-of-mass frame, and is given by $\beta_i=P_i/E_i$ where

$$E_i=\frac{E_{\text{c.m.}}^2+m_i^2-(m_j+m_k)^2}{2E_{\text{c.m.}}}, \tag{2}$$

and $E_{\text{c.m.}}$ is the total c.m. energy. Table I shows the maximum laboratory scattering angle for all three particles as a function of incident beam energy. In order to make a kinematically complete measurement of this reaction it is necessary to detect two of the outgoing particles. We decided to detect the nucleons for two reasons. First, the geometry of the jet target assembly and of the experimental site makes it difficult to design a detector system which would allow direct detection of the pions over their full angular range, whereas the restricted laboratory angle for the nucleons reduces the physical size and cost of the detectors. Second, a large fraction of the lowest energy pions would decay before reaching a suitable pion detector.

B. Accelerator requirements

The experiment was performed at the ‘‘T’’ site of the IUCF Cooler Ring where the beam undergoes a 6° bend. In its original configuration the T site contained two small 3° bending magnets with narrow gaps that did not permit a satisfactory detection of reaction products. We constructed and substituted a large-gap 6° magnet, which functions both as a ring bending dipole and as a low resolution spectrometer. The entrance aperture of this magnet is 12.5 cm high by 19 cm wide. This arrangement is shown in Fig. 2. Since the magnetic rigidity of the reaction protons is approximately half that of the beam, a reaction proton emerging at 0° will be bent by about 12° while the unscattered beam protons are only bent by 6°. Neutrons will of course not be deflected at all. This experimental geometry allowed measurement of all reaction products down to $\theta=0°$. Reaction protons could be detected over a range from about 3° to the right of the beam to 17° to the left of the beam.

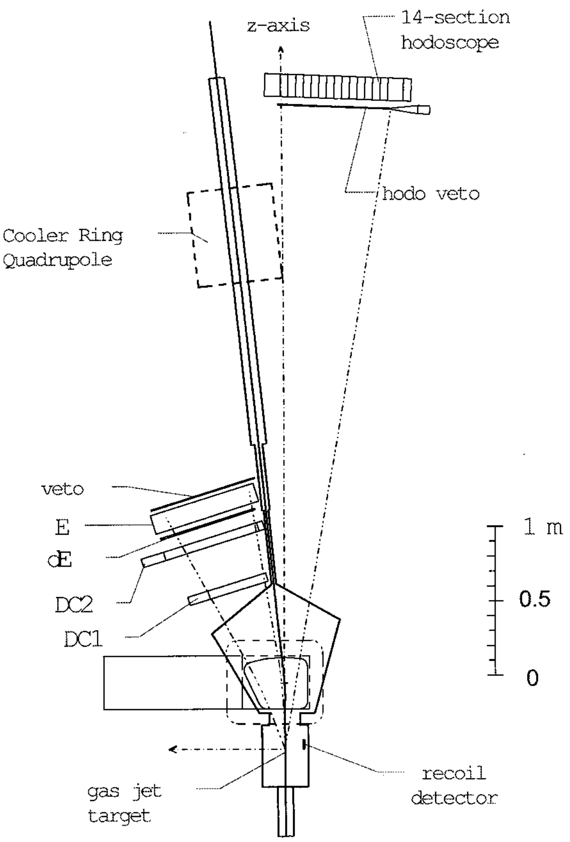

FIG. 2. Top view drawing of the CE03 detector stacks at the IUCF Cooler T site. DC1 and DC2 are the (x,y) drift chambers. The detectors called ΔE, E, neutron hodoscope, and veto are all plastic scintillators. The recoil detector is a position-sensitive solid state detector mounted inside the first pumping stage of the gas jet target. As our coordinate frame we choose the z axis in the beam direction at the target. The x axis is chosen to point towards the center of the Cooler Ring, and y points up, out of the page. We take the origin to be at the center of the jet target. The center of the 6°, large-aperture magnet is located at $z=44$ cm.

Threshold measurements place special requirements on accelerator performance. The strong energy dependence of pion production cross sections near threshold requires a small incident energy spread and a stable central beam energy. Schillaci, Silbar, and Young [7] predicted a total cross section for $pp\rightarrow pn\pi^+$ of about 1 μb and an energy dependence of $d\sigma/dE=0.5$ μb/MeV for a beam energy of 294.3 MeV (2.0 MeV above threshold). The IUCF Cooler ring provides a beam energy resolution of about $\Delta E/E=10^{-4}$ and is also stable to this level of accuracy. This translates into an inherent error of 0.01 μb at our lowest beam energy. A more serious systematic error in beam energy arises from any uncertainty in the ring circumference. The beam velocity is given by

$$\beta=\frac{Lf}{Hc}, \tag{3}$$

where β is the velocity of the ring protons, L is the ring circumference, f is the ring rf frequency, H is the ring harmonic (i.e., how many beam bunches are stored in the ring), and c is the speed of light. The present experiment determined a ring circumference of 86.78±0.02 m from the n and p opening angles at 294.3 MeV. The error implies an uncertainty of $\sigma_E=0.14$ MeV in the beam energy. This independent check is in excellent agreement with other recent ring calibrations. For the current experiment, the systematic energy error is significant only at our lowest energy.

C. Target chamber and exit foils

For 294 MeV the reaction protons have a laboratory frame kinetic energy of about 70 MeV and lose roughly 0.8 MeV in pumping baffles, vacuum chamber exit foils, and air before reaching the ΔE and E detectors. The reconstruction of the pion center-of-mass angle is sensitive to multiple scattering and to the accuracy of the nucleon energy measurements, and so it was important to minimize the amount of material between the target and the proton detector stack. An overhead view of our detector system is shown in Fig. 2. We used the IUCF gas jet [9], which provides a pure, thin target of molecular hydrogen with no detectable heavy impurities. It produces negligible straggling of the reaction protons and avoids the need to subtract background contributions from target cell walls. The disadvantage of this type of target is the difficulty of measuring its thickness accurately. Simultaneous measurements of the pion production and of the (known) pp elastic scattering cross section were used to normalize our pion cross sections. The luminosity monitor is discussed in more detail in Sec. III B.

Immediately downstream of the target, between the poles of the 6° magnet, is the ‘‘magnet vacuum chamber.’’ It allows the reaction protons to travel in vacuum for about 70% of their 1.5 m flight path. The proton exit foil was constructed of Kevlar cloth overlaid with two thin, differentially pumped Kapton foils, for a total thickness of 18.6 mg/cm^2. Along the flight path there were three thin vacuum pumping baffles, which served to divide the target chamber into differential pumping regions. These foils were constructed of thin aluminum and provided an additional absorber up to 20.6 mg(Al)/cm^2 for reaction protons scattered at angles larger than 4°. The total mean multiple scattering angle of reaction protons was 0.2°. The neutrons passed through a 686 mg/cm^2 aluminum window and then through 3.5 m of air on their way to the neutron detectors.

D. Wire chambers

We used two (x,y) multiwire drift chambers (DC1 and DC2) to track the reaction protons after they had passed through the magnetic field of the 6° magnet. These horizontal drift chambers employed a design previously used at Brookhaven [32]. Each consists of four wire planes, where the first two planes are used for the x and the second two for the y measurement. For each pair of planes there is a one cell offset between the sense wires in the first plane and the sense wires in the second plane. The dual timing signal removes the left-right ambiguity of a single plane and improves position resolution. The gas mixture used was 50% argon and 50% isobutane. The two drift chambers DC1 and DC2 were separated by 35 cm. They had a test bench position resolution of 0.25 mm [full width at half maximum (FWHM)]. During the experiment the resolution was close to 0.3 mm, leaving the chambers capable of determining the direction of the proton momentum to an accuracy of 0.07°. This resolution is considerably better than the 0.2° standard deviation in measured laboratory angles arising from multiple scattering; so the chamber resolution was indeed sufficient.

For a valid event, signals from eight cells (four pairs of wires) were required. The wire chamber efficiency was monitored continuously during the data runs by computing the ratio between the number of events firing three pairs and the number of events with four pairs providing a valid signal. Chamber efficiency was slightly time dependent. The deduced efficiencies per plane ranged between 98.5% and 95%. The simultaneous measurement of luminosity and reaction count rate with the same detectors largely avoids the need for this and similar efficiency corrections, e.g., dead time. However, differential counting losses can still be appreciable. In a detailed off-line analysis it was found that the lower energy $pp \rightarrow pn\pi^+$ events were always detected more efficiently than the fast pp elastic events, which are used for the luminosity monitor. Our final luminosity analysis corrected for this and also excluded events that fell into the cells nearest the beam pipe, because fortuitous coincidences from high energy background distorted the ratio of monitor and reaction protons [33].

E. Detector stacks

As shown in Fig. 2, the CE03 apparatus consists of two sets of detectors mounted on opposite sides of the beam pipe. The detectors on the inside of the Cooler Ring detect protons; those on the outside of the ring detect neutrons. The proton arm detector stack consists of the drift chambers DC1 and DC2, followed by a thin ΔE detector. To permit fast (mean) timing the large, 3-mm-thick ΔE detector is viewed by two adiabatic light pipes mounted at opposite ends of the scintillator and by fast Amperex 2020 phototubes. The signals from this detector were used to start the event timing circuits. The ΔE detector is followed by a stack of five full energy measuring (E) detectors each of dimension $12.7 \times 7.62 \times 71.12$ cm^3, viewed by 7.5-cm-diam Hamamatsu 1911 phototubes from their smallest face. This 12.7 cm thickness stopped all $pp \rightarrow pn\pi^+$ reaction protons in this experiment. The proton arm detector system was backed by two thin veto paddles used to discriminate between protons from pp elastic events (which punched through the E detectors) and the lower energy reaction protons from $pp \rightarrow pn\pi^+$ which stopped in the E detectors.

In addition to the forward detector stacks we also utilized a silicon position-sensitive recoil detector (PSD) mounted inside the target chamber at an angle of about 80° from the target center. This detector provided a coincidence trigger with the forward proton arm and was used to determine the luminosity and the gas jet profile. The luminosity monitor is discussed in detail in Sec. III B.

The neutron detector was preceded by a veto detector, which consisted of a set of four rectangular scintillators. They are identical in shape to those in the proton arm and discriminated between charged particles and neutrons entering the neutron hodoscope. The hodoscope consists of 14 scintillator bars of dimension $5 \times 15 \times 120$ cm^3 with a 20 cm light pipe and an Amperex XP2252H phototube mounted at each end. Its performance has been reported earlier [34]. These bars were mounted with their longest dimension vertical to permit positioning the hodoscope very close to the beam pipe, and measured neutron angles down to 0°. The position resolution in the y direction (along the length of the bars) was ~3 cm (FWHM). All scintillator bars were equipped with a fiber optic coupling connected to an ultraviolet laser. This allowed us to monitor the detector gain and to set the coincidence timing among scintillators. At the lowest three beam energies, the $pp \rightarrow pn\pi^+$ reaction particles were confined to a small enough kinematic cone so that a single hodoscope location adequately sampled the entire pion phase space. For the higher energies the hodoscope had to be moved (once) in order to cover the full angular neutron range. (The largest angle required was 16.8°.) We called these geometries the ''in'' and ''out'' positions, respectively. The proton detectors had sufficient solid angle to cover the θ range of interest for all situations.

F. Event identification and triggering

The electronics for CE03 used a two-level trigger based on the LeCroy 2372 Memory Lookup Unit (MLU). The first level fast trigger used discrete NIM logic modules to determine if a potential event of interest had occurred. This decision required a coincidence between the ΔE and the E detectors *or* a coincidence between the top and bottom photomultipliers of a particular hodoscope bar. If this trigger was satisfied, the analog-to-digital converter (ADC) gates would be opened and the time-to-digital converters (TDC's) started. The fast trigger generated a strobe for the MLU and also closed the ''busy'' gate, preventing another event trigger before the current one was completely processed. The MLU took its input from the E, ΔE, hodoscope, and veto detectors. It was programmed to categorize four event types based on the signal pattern from these detectors. With this arrangement we sorted protons or neutrons in the neutron arm, $pp \rightarrow pn\pi^+$ events, energetic (punch through) protons in the proton arm, and the laser pulses used for calibration. Events triggering only the proton arm were further sorted into those coincident with the PSD detector (pp elastic protons) and those with no PSD signal. Since the PSD detector was an order of magnitude slower than the scintillators, this discrimination had to be done using discrete logic after the MLU output was generated. If the event pattern did not match any of the defined events, the MLU would generate a fast clear signal for all ADC's and TDC's and hold the ''busy'' gate for an additional 2 μs to allow the system to reset. The design of this system allowed event triggers to be rapidly reconfigured. Flexibility of trigger definition, particularly for the veto detectors, proved to be extremely useful in detector calibration and in measuring detector efficiencies. Hardware event processing took 2 μs if a second level trigger was not satisfied and ~300 μs if an event trigger was generated. Any events which were read out were buffered locally [in a microprogrammed branch driver (MBD)] and transferred to the analysis computer when the buffer became full. Buffer transfers typically took 3 ms. When all processing and transfer times are considered, our event rate was hardware limited to 0.8 kHz. We typically ran with a dead time of 15%.

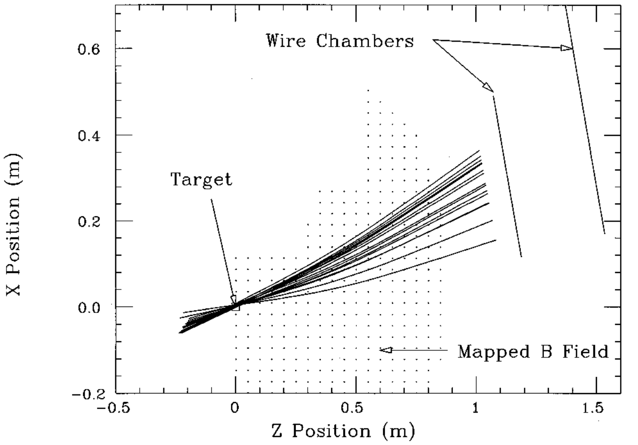

FIG. 3. Projection onto the (xz) plane of pp elastic proton trajectories through the 6° magnet at 299.3 MeV. The tracks are reconstructed starting with the two measured positions in the wire chambers and are traced back to the target through the magnetic field (the shaded area indicates the mapped portion). The tracks shown are from pp elastic scattering from the gas jet centered at $z=x=0$ cm. Reaction protons from $pp\rightarrow pn\pi^+$ would have about twice the bending in the magnetic field due to their lower magnetic rigidity.

At 294.3 MeV the large (mostly elastic) proton flux in the neutron and proton detectors generated about 10 000 potential random coincidences for each true $pp\rightarrow pn\pi^+$ event. Tests showed that the second level triggers (MLU) were 99.5% efficient in removing this background. The remaining background was successfully removed by appropriate software cuts that will be discussed in Sec. III A. The overall efficiency of background elimination was determined by a data run taken at 290 MeV, 2.3 MeV below the $pp\rightarrow pn\pi^+$ production threshold, but still above those for $pp\rightarrow pp\pi^0$ and $pp\rightarrow d\pi^+$. Analysis of these runs shows that *no* spurious events survive the full set of hardware and software cuts.

III. CALIBRATION AND ANALYSIS

A. Data cuts

Several types of background events are not suppressed by hardware triggers, e.g., the accidental coincidences of uncorrelated protons and neutrons, or quasielastic scattering from walls and impurities. Particularly at 294.3 MeV where the pion production cross section is very small most fast triggers are spurious. We found a set of three software cuts which completely eliminated these undesired events. The first cut was based on tracking detected protons back through the 6° magnet to the target plane. Figure 3 shows a view of reconstructed particle trajectories from elastic scattering for 299.3 MeV protons. The location of the gas target nozzle is defined as $z=0$. This figure shows that valid tracks form a focus at the target, provided that their energy is assigned correctly. (Elastically scattered protons do not stop in the E detectors and their energy has to be calculated from the angle measured by the drift chambers.)

By design only highly inelastic protons, e.g., those in the $pp\rightarrow pn\pi^+$ event stream, stop in the E detector and produce a full energy signal. Elastic and energetic background protons do not stop and deposit only a fraction of their energy. This has the advantage that energetic protons that produce spurious $pp\rightarrow pn\pi^+$ triggers will be assigned an erroneously low energy and thus a smaller radius of curvature in the magnetic field. Only events of interest will have tracks that pass through the target (at $x=y=z=0$). Straggling and resolution produce a focus of about 1 cm in diameter as shown in Fig. 4. This figure displays the (x,y) coordinates and the intensity of potential $pp\rightarrow pn\pi^+$ proton tracks intersecting the $z=0$ plane for the 299.3 MeV run. The dense spot near $(x=0,\ y=0)$ is due to true $pp\rightarrow pn\pi^+$ events that are traced back with the correctly assigned energy while the diffuse cloud of events at large x is background from energetic protons in spurious coincidences. Thus the ray trace permits a good separation between $pp\rightarrow pn\pi^+$ events and background coincidences, allowing the latter to be removed from further processing.

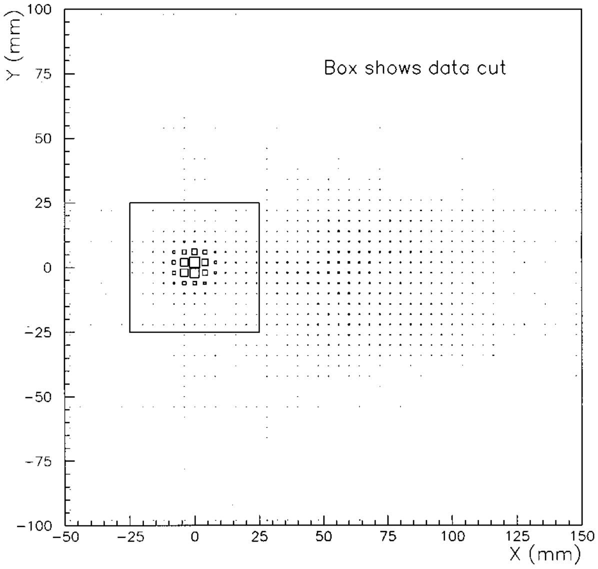

FIG. 4. Distribution of potential $pp\rightarrow pn\pi^+$ events (pn coincidences) traced back to the target plane $z=0$ before any software cuts are applied (see Fig. 2 caption for coordinate definition). True $pp\rightarrow pn\pi^+$ events should focus near (0,0) while the background events triggered by energetic protons that do not stop in the E detectors form a diffuse ''cloud'' at larger values of x. A software cut applied around the dense $pp\rightarrow pn\pi^+$ spot, as shown by the box, would remove background caused by protons with energies above about 150 MeV.

The second cut employed is based on conventional particle identification, i.e., on the E vs ΔE relation for a stopping proton. In Fig. 5 we show the relationship between the E detector signal and the ΔE detector signal for possible $pp\rightarrow pn\pi^+$ events at 319.2 MeV in the absence of any software cuts. Protons that stop approximately follow the relation $\Delta E\sim 1/E$, but the background from energetic punch-through protons produces a smaller ΔE signal that changes little. The separation between the pion production events and the background permits a cut that provides a powerful supplement to the ray trace cut previously discussed, allowing both of them to be generous. A Δt cut on the time difference between the neutron and proton detector stacks serves to eliminate a number of accidental coincidences which have a low energy proton produced in one beam bucket and an uncorrelated neutron in the next one. These

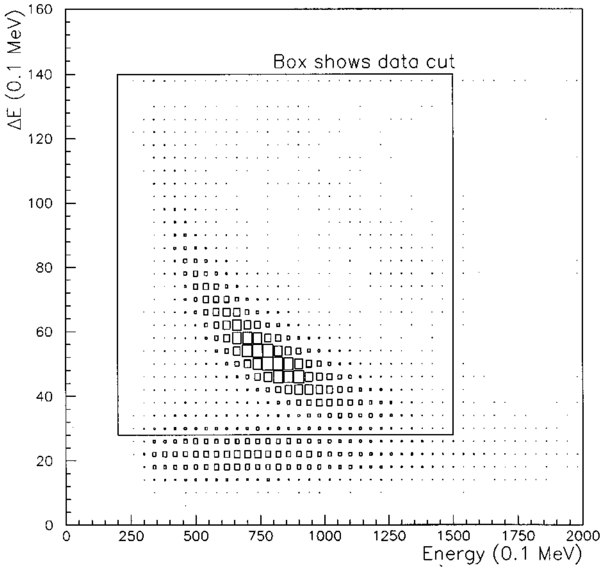

FIG. 5. Plot of raw data at 319.2 MeV beam energy for ΔE vs E values of protons from p-n coincidences before software cuts are applied. The lower band (outside the box) is primarily accidental pp elastic and quasielastic background; the bright middle band is the true $pp \rightarrow pn\pi^+$ locus. The faint upper right group is caused by $pp \rightarrow pn\pi^+$ events where both the p and the π^+ were detected in the proton arm. Real events have proton energy between 37.7 and 130.1 MeV. The cut for the accepted events applied for the final analysis is shown by the box.

three cuts together serve to completely eliminate background from our sample of pion events. Figure 6 shows the missing mass spectrum at 294.3 MeV, computed from the measured neutron and proton four-momenta, before and after applying the three software cuts discussed. The comparison shows that we lose no events in the pion peak but that all of the background is removed. The small low energy tail which survives the cuts is due to nuclear reactions in the E detector resulting in reduced light output. In the final analysis a missing mass cut at 130 MeV was also used and small cut corrections have been applied.

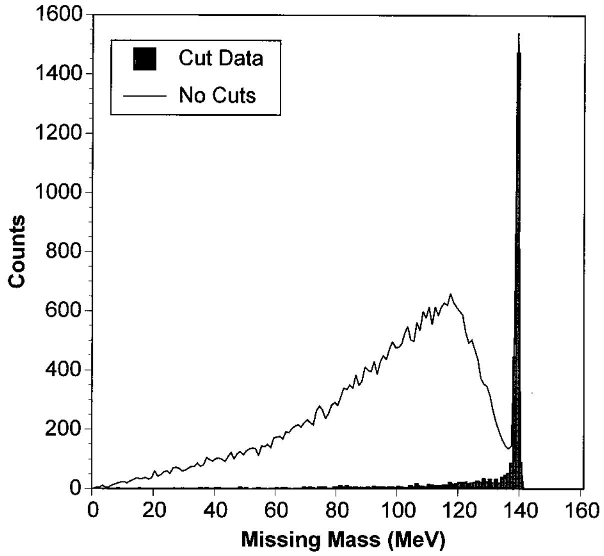

FIG. 6. Comparison of π^+ missing mass spectra for analysis with and without the three primary software cuts as described in the text. The small low energy tail of the cross hatched spectrum that has survived the software cuts is caused by nuclear reactions in the E scintillator. In the final analysis a missing mass cut at 130 MeV, and an appropriate correction for losses, were used.

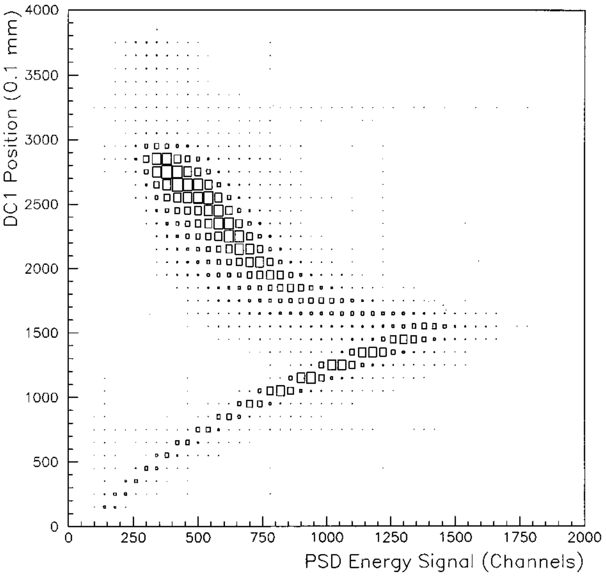

FIG. 7. Two-dimensional plot for the luminosity monitor. Counting intensity is shown as a function of the (recoil) energy deposited in the PSD detector and the position of forward scattered protons (~scattering angle) in drift chamber DC1. The recoil energy increases rapidly with scattering angle. The point at which the recoil protons punch through the PSD (~channel 1300) provides a check on either the PSD thickness or on its position.

B. Luminosity

For internal target experiments in storage rings the traditional methods of determining luminosity via known target thickness and integrated charge will not work. Instead we measure luminosity by making a simultaneous measurement of pp elastic scattering, and comparing it with the published cross sections. Using the relation

$$\Delta N_0 = \mathcal{L}\frac{d\sigma}{d\Omega}(\theta)\Delta\Omega, \tag{4}$$

where ΔN_0 is the number of observed counts, $\mathcal{L}$ is the time-integrated luminosity, $d\sigma/d\Omega$ is the pp scattering cross section, and $\Delta\Omega$ is the effective solid angle, we can solve for the luminosity if $d\sigma/d\Omega$ is known. We measured pp elastic scattering by selecting coincidences between the forward protons with θ_{lab} between 5° and 17° and a PSD of dimension 4.5×0.7 cm^2 covering the corresponding recoil scattering angles. The ϕ range accepted is sharply defined by the PSD, but the coincidence acceptance varies smoothly with θ for the extended gas target. Figure 7 shows the DC1 position ($\sim\theta$) of the forward scattered proton as a function of the energy deposited in the PSD detector. For small forward scattering angles the detected recoil proton has very low energy and stops in the PSD. For larger forward angles the coincident recoil protons begin to punch through the

PSD, and the deposited energy drops off with increasing angle.

High background during beam injection caused some radiation damage and a slow deterioration of the PSD. Therefore, its performance was measured before and after the runs using an alpha source. In order to cross-check the PSD performance and the calculated luminosity monitor coincidence acceptance, comparisons between *pp* elastic rates with and without the PSD coincidence requirement were made in a 120 MeV run. (At 120 MeV elastic protons stop in the E detector and the 120 MeV peak with about 2.5% FWHM resolution is clearly distinguishable from background. However, a similar operation was not possible for 300 MeV protons that do not stop.) Counting losses arising from poor charge collection and noise were small, except for the smallest pulse heights. Any error attributable to the PSD was less than 6%. We assign a systematic error of 6%.

The most significant correction to the (coincident) luminosity measurement came from the extended tails of the jet target. By far the highest gas density is found within 3 mm of the jet center, but the diffusion tails extend to $|z| = 7.8$ cm and add significantly to the overall luminosity. The $pp \rightarrow pn\pi^+$ forward detectors are located 1.5 and 4.5 m away near the z axis and therefore see all of the illuminated gas target, including its upstream and downstream tails. In contrast, the PSD is located at about 80° to the beam axis, only 11.7 cm from the jet; therefore, only the central 6 cm of the gas target can be monitored with a coincidence requirement. A Monte Carlo simulation using the measured central gas target distribution (with modeled tails) tracked the correlated protons through the detector geometry to determine its acceptance. This calculation is not difficult because at the target the beam has a diameter of only about 1 mm so that the (illuminated) jet can be modeled as a function of z only. For the best fit to the observed jet shape and the partially observed tail (see Fig. 8), we find that the luminosity monitor sees only about 70.5% of the distributed gas target seen by the large detectors. Based on fits with alternate ''reasonable'' models for the jet tail we assign a 7% systematic model error for the acceptance.

A smaller, but not negligible source of error in the luminosity comes from the uncertainty of the *pp* cross section itself. We used the VPI [35] phase-shift-fitting program SAID to generate the *pp* cross section curves for our energies and angular ranges. A 4% uncertainty was used for the published *pp* elastic cross section. Figure 9 shows a comparison of a typical *pp* elastic cross section distribution with the 1994 SAID solution. Only recoil angles between 75° and 80° were used in the final luminosity determination.

The target thickness was adjusted to about 2×10^{15} atoms/cm^2 to optimize the data taking rate. In order to reduce beam loss due to multiple scattering, the jet was turned off during the injection, acceleration, and reset phases of the cycle. Typical luminosities were about 2×10^{30} cm^{-2} s^{-1} just after the jet was turned on and fell exponentially during the time the jet was on. The optimal cycle lasted 2 min and used a 1 min target-on period for each beam cycle. About 20% of the original beam was dumped at the end.

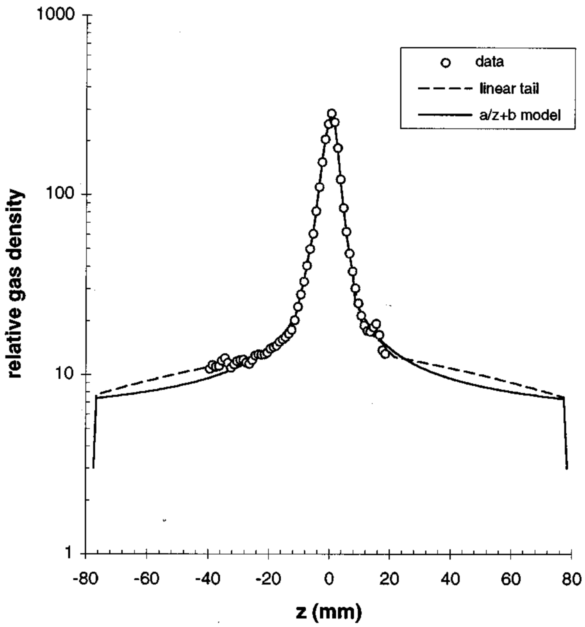

FIG. 8. Comparison of the observed portion of the gas jet distribution (open circles) as determined by *pp* elastic scattering and the extrapolated distributions using two different models. The gas density drops to negligible values past the pumping baffles located at $|z| = 7.8$ cm. The lower curve was used for the distribution in the Monte Carlo calculations; the difference between the curves yielded an estimate for our model error.

Plastic scintillators in both the proton energy (E) detector and the neutron hodoscope were used to measure deposited energies. The hodoscope pulse height spectrum is not used to measure the neutron energy, but the pulse height threshold enters directly into the determination of the neutron detection efficiency. The calibrations of both detector systems are crucial to our results and their interpretation (see Sec. III E). The neutron hodoscope was calibrated using low energy *pp* elastic scattering (120 MeV), cosmic rays, and directly injected light from an ultraviolet laser. The amount of laser light admitted was controlled by a set of calibrated neutral density filters. The laser provided six to eight calibration points defining the electronic offsets and the relative pulse height response to light levels. The scale of the calibration

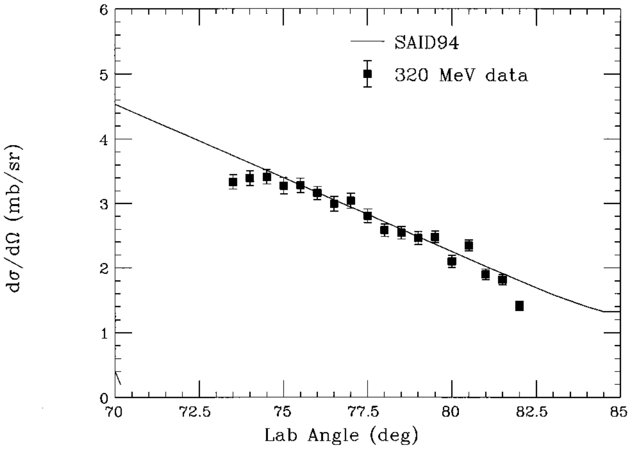

FIG. 9. The *pp* elastic scattering cross section obtained from the luminosity monitor, after correction for acceptance, is shown as a function of recoil angle for 319.2 MeV beam and compared with the SAID94 *NN* phase shift solution. Only recoil events between 74° and 80° were used to determine the luminosity. The cutoffs in the data at 72° and 82° are due to limits of the detector acceptance.

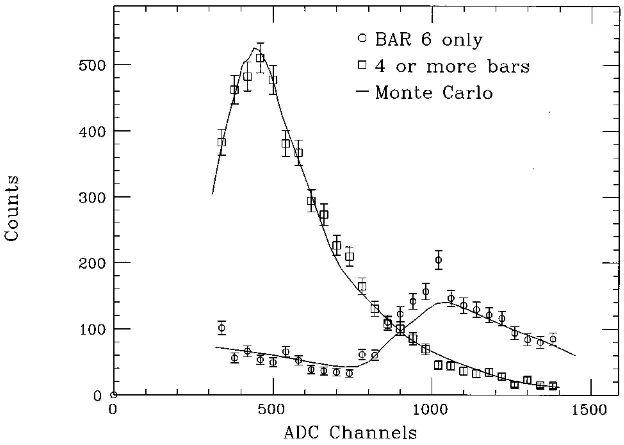

FIG. 10. Typical spectra of energies deposited in the hodoscope by selected cosmic ray events that either fire just a single scintillator at oblique incidence or else four or more bars (at near normal incidence). The hodoscope energy calibration was set by matching the Monte Carlo calculations (curves) as described in the text. This measurement provides an absolute energy vs pulse height calibration close to the software pulse height cut for each scintillator bar in the neutron arm.

was determined by detecting cosmic rays in all bars and was cross checked by 120 MeV *pp* elastic scattering in a number of bars. Cosmic ray data were taken throughout the experiment with the scintillator bars oriented vertically. By grouping these events by angle of incidence into two classes (those that fired only one hodoscope bar and those that fired four or more bars) the cosmic rays provided two energy calibration points. The deposited energy differed considerably for these two cases and a Monte Carlo calculation predicted energy distributions for both situations, as shown in Fig. 10. We were able to determine the hodoscope pulse height calibration near the 9.6 MeV threshold point to ±0.5 MeV.

Monte Carlo calculations showed that the reconstruction of the pion momentum is very sensitive to the energy of the detected nucleons. The E detectors were calibrated using *pp* elastic scattering, cosmic rays, and the reaction protons from $pp \rightarrow pn\pi^+$. The *shape* of the proton energy distribution depends on the details of the πNN reaction but the end points are determined entirely by conservation of energy and momentum. Therefore we measured the end points for each of our beam energies and compared with the kinematically determined values. Combining this with *pp* elastic scattering at 45 and 120 MeV, and with cosmic ray data, we were able to calibrate the E detectors to better than ±0.5 MeV for beam energies of 294.3 and 299.3 MeV, and to better than ±1.0 MeV for 306.3, 314.1, and 319.2 MeV.

C. Neutron time-of-flight and detection efficiency

We used time-of-flight techniques to determine the neutron energy. The proton detector can be utilized as a start detector if a proton time-of-flight correction is made. If the proton momentum p_p and flight path d_p, the neutron flight path d_n, and time difference Δt_{pn} are known, the neutron velocity can be determined from the expression

$$\beta_n = \frac{d_n p_p}{d_p E_p - (\Delta t_{pn} + \delta) c p_p}, \tag{5}$$

where δ is a measurable constant which depends on the electronics, cabling, and photomultipliers, but not on any of the particle kinematics. Using this equation, time differences, the measured proton energy, and the detector geometry, we can compare the extracted neutron energy distribution to that predicted by our (s-wave) Monte Carlo calculation. Figure 11 shows this comparison at 299.3 MeV. Fine adjustments for the neutron energy calibration were made by calculating the kinematically determined energy centroids separately for each bar and comparing them with the observed centroids.

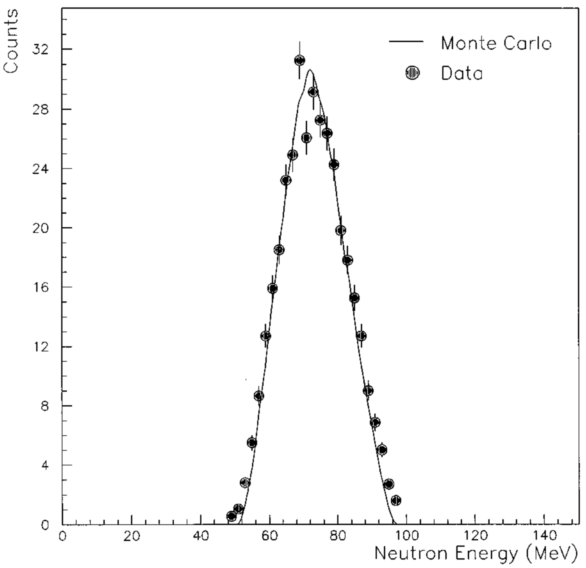

FIG. 11. Neutron energy distribution as measured by time of flight at a beam energy of 299.3 MeV. Data are compared with a Monte Carlo prediction (including FSI) of the expected energy distribution based on $pp \rightarrow pn\pi^+$ kinematics.

The neutron detection efficiency depends on the geometry and composition of the detectors, the energy of the neutrons, and the detector energy threshold. We used the neutron efficiency code from Kent State [36] to compute and integrate the neutron detection efficiency over our measured neutron energy spectrum. The detection efficiency shown in Fig. 12 was calculated for a beam energy of 294 MeV as a function of the threshold for the neutron detector pulse height (which has a known relation to the deposited energy). For a threshold near 10 MeV (electron light equivalent) the detection efficiency does not change significantly for the beam energies used in this experiment. The individual neutron hodoscope bars had hardware energy thresholds up to 9 MeV. We used a uniform software cutoff at 9.6 MeV to regularize the weighting of the bars. With this threshold, the neutron detection efficiency is found to be (0.141±0.005) where the error comes from the uncertainty in the hodoscope threshold energy calibration. In addition, Cecil, Anderson, and Madey [36] suggested an estimated scale uncertainty of about 5% in neutron detection efficiencies determined from this code. (Other tests have consistently shown errors under 10%.) Combining experimental and model uncertainties we assign an 8% hodoscope contribution to the absolute scale error.

D. Detector acceptance and final state interactions

Despite an experimental acceptance of up to 40%, Monte Carlo calculations for the coincidence acceptance are re-

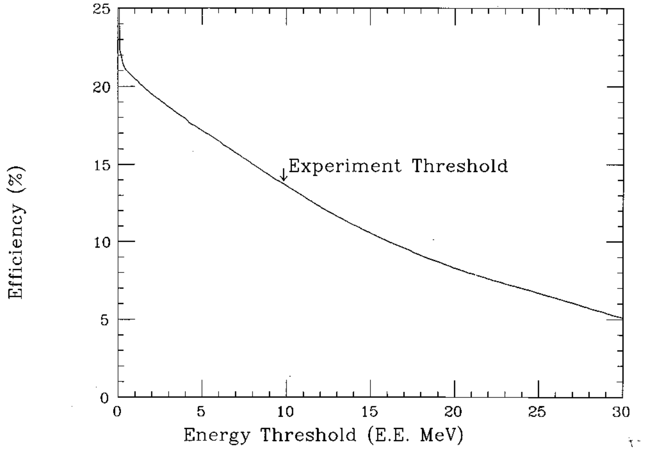

FIG. 12. Computed neutron detection efficiency, integrated over our observed neutron energy spectrum, as a function of neutron detector pulse height threshold. The chosen software threshold cut for this experiment is shown by the arrow; it is at 9.6 MeV (electron light equivalent).

quired because the percentages of reaction nucleons accepted for different parts of the phase space can differ significantly; e.g., few events with both nucleons on the same side of the beam line are detected. Therefore, a calculation of the $pp \rightarrow pn\pi^+$ detector acceptance for the three-body final state requires a Monte Carlo simulation of the experiment. The simulation included an accurate computation of reaction phase space and particle trajectories to account properly for the varying acceptance. Event reconstruction is also affected by the energy and angle measurements; hence, the simulation took explicit account of the B field, scattering centers (foils), some energy losses, and all detector resolutions. Adopting the method used for IUCF experiment CE01 [37] we used the final state interaction (FSI) model proposed by Watson [38] and later modified by Migdal [39] and Morton *et al.* [40] when calculating the observables involving the pion. In this model the $pp \rightarrow pn\pi^+$ interaction is viewed as a sequential process: First, the pion is produced by one of the nucleons; then, the two nucleons interact with each other for a long time afterward. The pion production is assumed to occur in a very short time. With this assumption, the pion distributions are determined by the πNN vertex of interest. However, while the center-of-mass motion of the two nucleons is also fixed at this time, their motion relative to each other (i.e., their opening angles) may be strongly modified by the FSI, the known n-p interaction at low energy. The model implies that the pion-nucleon final state interactions are weak enough not to significantly affect the pion angular distribution. Thus, the pion momentum is fully determined by the measured four-momenta of the reaction neutron and proton.

Empirical evidence for the need to include the nucleon-nucleon FSI was found in various ways. The deduced angular distributions must not depend on detector positions and must be continuous. Similarly, the reaction total cross section must be independent of the way it is measured provided the acceptance calculation is correct. All pion angles are sampled in both the ''in'' and ''out'' hodoscope geometries (see Sec. II E). If the pion differential cross section is calculated with the standard (no FSI) Monte Carlo acceptance and integrated to obtain $pp \rightarrow pn\pi^+$ total cross sections for each of the two geometries used to obtain 319.2 MeV data, the two results differ by three standard deviations. Similarly, two pieces of the neutron angular distribution (in coincidence with the reaction proton) are separately measured by the two hodoscope geometries. Use of the acceptance calculation with no np FSI results in a discontinuity at the interface of the two parts of the distribution. (The same effect can also be seen by arbitrarily subdividing the hodoscope at some x coordinate and analyzing the two pieces independently.) These disagreements are the result of an incorrect acceptance calculation because the shape of the spectra outside the angles measured by the detectors is calculated incorrectly. Only for an adequate FSI interaction will the distribution be continuous across a boundary between two detector geometries (artificial or real) and will the total extracted cross section be the same for the two sets of data mentioned above. By construction, the FSI model used does not change the observed pion distributions; the effect of this FSI calculation is to scale the n-p coincidence efficiency which affects the deduced cross sections by accounting for the relative angular distribution of the nucleons.

The FSI correction of Watson and Migdal does not affect the pn invariant mass distribution because the correction is based on the s-wave pn cross section which depends only on the pn total energy.

The strength of the final state np interaction differs for triplet and singlet states, and the relative contribution of each is not known *a priori* for the continuum interaction sampled here. A variation of singlet to triplet state weight in the FSI calculation indicated that the best fit to the ''matching'' conditions discussed above is obtained when the ratio of singlet to triplet state strengths is close to the statistical mix (1:3). However, this is not a sensitive parameter since for the hodoscope in the small-angle (''in'') position the FSI correction to the total cross section stays below 4% for most energies. In matching cross sections measured with different hodoscope positions we find a broad χ^2 minimum as the triplet component is changed from 65% to 85%. In the final acceptance calculation, we use 75%. Except for 320 MeV, the effect of the triplet/singlet mix on the pion cross sections is weak. Figure 13 shows Monte Carlo predictions of the (coincident) event distributions for the proton laboratory angle at 319.2 MeV with and without FSI. The curve with FSI predicts stronger forward peaking in the *nucleon* cross section, and correspondingly, a stronger forward and backward peaking in the pion c.m. acceptance. For our apparatus, the inclusion of the FSI decreases the deduced total pion production cross section by about 30% when only the ''in'' geometry at 319.2 MeV is used, but by less than 8% when all p and n angles are sampled in the apparatus, as was done in this experiment. The change in the pion cross section is about 4% at the lowest energy. A comparison of the acceptance calculation with the proton angle spectrum measured at 299.3 MeV is shown in Fig. 14. Although agreement is expected only if the pure s-wave assumption in this particular phase space calculation is correct, it will later be seen that the interaction at 299.3 MeV is predominantly s-wave.

E. Event reconstruction

This experiment directly determines the four-momentum vectors of the reaction proton and the neutron. From this we reconstruct the pion four vector as

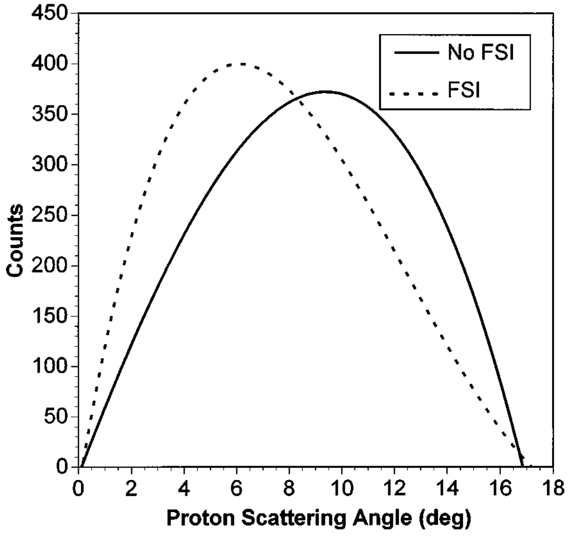

FIG. 13. Monte Carlo study of the effect of *NN* final state interactions on the proton angular distribution at 319.2 MeV. The magnitude of the FSI effect depends on angle and energy, but is always significant.

$$p_\pi^\mu = p_{\text{beam}}^\mu + p_{\text{tgt}}^\mu - p_p^\mu - p_n^\mu. \tag{6}$$

We studied the sensitivity of the pion four-momentum to both systematic and random errors in the measured proton and neutron vectors. Figure 15 shows the relative change in pion c.m. angular distribution at 299.3 MeV when various systematic errors are introduced. The systematic errors have a large effect at 294.3 MeV and a significantly smaller effect at the higher incident beam energies. Figure 15 gives the results for a systematic -0.5 MeV proton energy error and a systematic $+0.5°$ proton angle shift. The effect of these shifts is demonstrated in Fig. 15 by dividing the ''defective'' angular distribution by the ''correct'' angular distribution. The observed sensitivity of the pion angular distribution to systematic shifts in proton (and neutron) energy demonstrates the need for a very careful energy calibration. At 294.3 MeV, this sensitivity is strong enough to require that the energy calibration be accurate to 0.5 MeV. Sensitivity to systematic errors decreases rapidly as the incident beam energy increases so that at 319.2 MeV there would have to be a systematic energy shift of -2.5 MeV to show the same distortions as in Fig. 15. The figure also demonstrates that we are an order of magnitude less sensitive to systematic angle errors. We find even less sensitivity to random errors. There are two primary reasons for the extreme sensitivity to proton or neutron energy: Near threshold a small change in nucleon energy is sufficient to significantly change the deduced pion scattering angle that conserves momentum. The time-of-flight calculation of neutron energy depends directly on the measured proton energy, and a systematic error in proton energy distorts both the proton and neutron energies in the same direction.

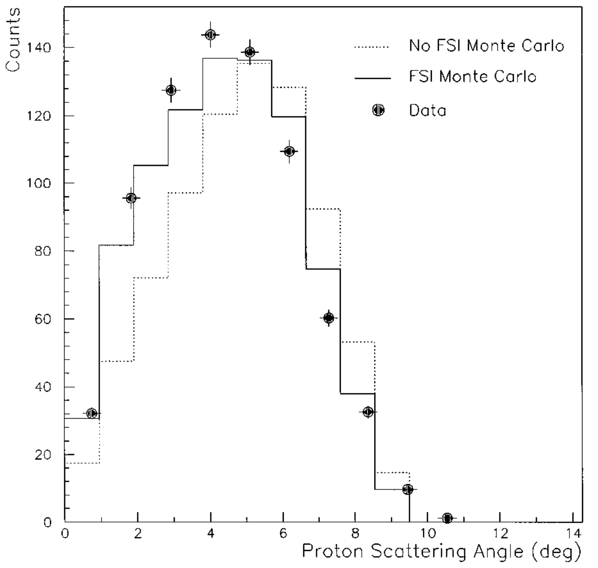

FIG. 14. Comparison of observed proton angular distributions at 299.3 MeV with Monte Carlo predictions. The more forward peaked Monte Carlo calculation includes the FSI interaction, the other calculation has the FSI turned off. The FSI correction is necessary to reproduce the experimental proton (and neutron) angular distributions.

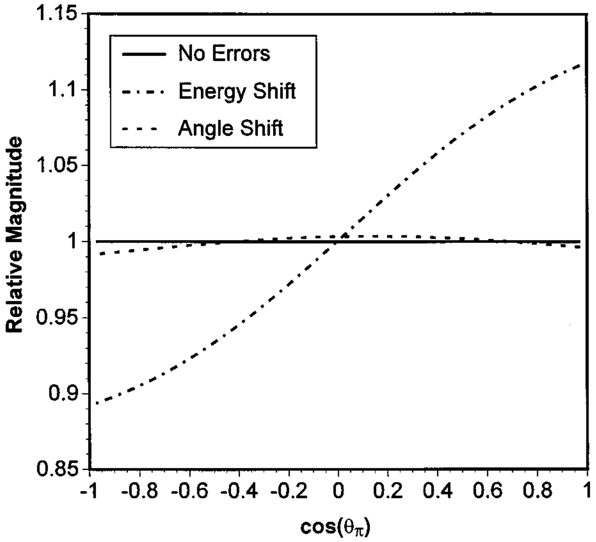

FIG. 15. Monte Carlo study of the effect of systematic energy and angle errors of the detected nucleons on deduced pion angular distributions in the three-body center of mass, at a beam energy of 299.3 MeV. The figure shows the ratio of the shifted (distorted) angular distributions divided by the correct angular distribution. The ''true'' proton energies were shifted by -0.5 MeV and the proton angles by $+0.5°$. Such errors are consistent with the upper limit on the experimental accuracy. The extracted pion angular distributions are much more sensitive to systematic energy errors than to systematic angle errors or to random errors of any kind.

F. Experimental errors

The cross section errors shown in Tables II and III include statistics and estimated errors from random and angle-dependent sources only. The scale errors were combined in quadrature and yield a common uncertainty of ±15% in the absolute normalization. The scale error is not shown in the figures. The contributions to this systematic error are dominated by uncertainties in the luminosity (11%) and the neutron detection efficiency (8%). Smaller contributions arise

TABLE II. Total cross sections for $pp \to pn\pi^+$. Errors shown in the table are the combined random errors for this measurement; all cross sections also have a common 15% absolute scale uncertainty, which is not included. There is a ±0.2 MeV uncertainty in the incident beam energy.

Beam energy (MeV)	η	σ_π (μb)	Random error (μb)
294.3	0.112	0.71	0.04
299.3	0.210	4.81	0.24
306.3	0.298	13.91	0.65
314.1	0.373	25.5	1.6
319.2	0.416	41.1	1.7

from the calculated coincidence acceptance, corrections for reaction tails, and detector geometries. Each bombarding energy quoted has a 0.2 MeV error, a negligible effect for all bombarding energies except the lowest.

The assigned scale errors reflect the estimated reliability of the models (e.g., jet tails, FSI effects) used in the extraction and calibration of the data. The luminosity scale error dominates. It can be improved in future experiments by using larger recoil detectors and by having some redundancy in the drift chambers. We note that for the analysis presented here we used a more detailed test of the drift chamber performance and a jet model different from that employed in a previous presentation of the data [14]. The reanalysis did not produce any changes in the angular distributions, and changes in the total cross section values were minor for all energies except for the 294.3 MeV point. The latter had to be reduced by about 25%.

TABLE III. Differential cross sections in units of (μb/sr) for $pp \to pn\pi^+$ in the c.m. frame. The errors shown combine the uncertainties from statistics with angle-dependent systematic errors arising from uncertainties in the energy calibration of the detectors.

294.3 MeV		
$\cos\theta_{\text{c.m.}}$	$d\sigma/d\Omega$	Error
−0.75	0.054	0.016
−0.25	0.058	0.011
0.25	0.060	0.011
0.75	0.056	0.016
299.3 MeV		
$\cos\theta_{\text{c.m.}}$	$d\sigma/d\Omega$	Error
−0.833	0.41	0.05
−0.500	0.39	0.04
−0.167	0.36	0.04
0.167	0.35	0.04
0.500	0.37	0.05
0.833	0.41	0.05
319.2 MeV		
$\cos\theta_{\text{c.m.}}$	$d\sigma/d\Omega$	Error
−0.889	4.21	0.44
−0.667	3.61	0.31
−0.444	3.15	0.25
−0.222	2.86	0.18
0.000	2.78	0.17
0.222	2.74	0.18
0.444	3.06	0.25
0.667	3.37	0.31
0.889	3.66	0.44

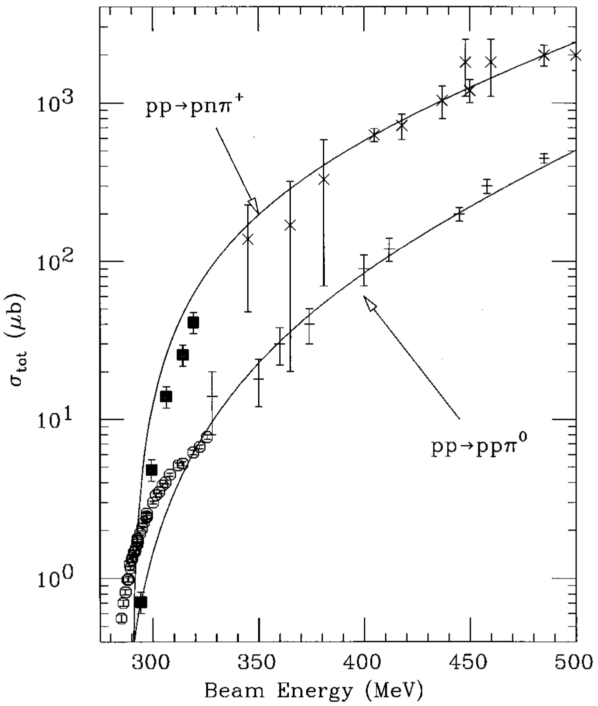

FIG. 16. Comparison of new $pp \to pn\pi^+$ data (solid squares with full errors shown) and recent IUCF $pp \to pp\pi^0$ cross sections (open circles) to earlier data. The curves are extrapolations to threshold of a simple parameterization of higher energy data by VerWest and Arndt.

IV. RESULTS AND DISCUSSION

A. Total cross sections

The total cross sections for $pp \to pn\pi^+$ presented in Table II are compared in Fig. 16 to previously published data for this reaction and for $pp \to pp\pi^0$ [41,9,10]. The new cross sections from the Indiana Cooler agree well with earlier data, which have much larger errors. However, an extrapolation of fits in the delta region (solid lines) based on Ref. [42] does not represent the threshold data well.

A more detailed comparison to the cross sections for other pion production channels is shown in Fig. 17 as a function of η, the maximum pion momentum. For this experiment, the lowest value of η is 0.112, corresponding to 2 MeV above threshold. In this case, the maximum pion kinetic energy in the c.m. frame is 0.86 MeV. The data shown for $pp \to pp\pi^0$ are from Meyer *et al.* [9] and from Bondar *et al.* [10]. For $pp \to d\pi^+$, we show the equivalent cross sections of Hutcheon *et al.* [13] for $np \to d\pi^0$ multiplied by the isospin factor of 2.0. The $pp \to pp\pi^0$ data approximately follow the s-wave phase space dependence (in detail, Coulomb corrections are also important [9]). The $pp \to d\pi^+$ total cross sections follow the s-wave η^1 phase space dependence close

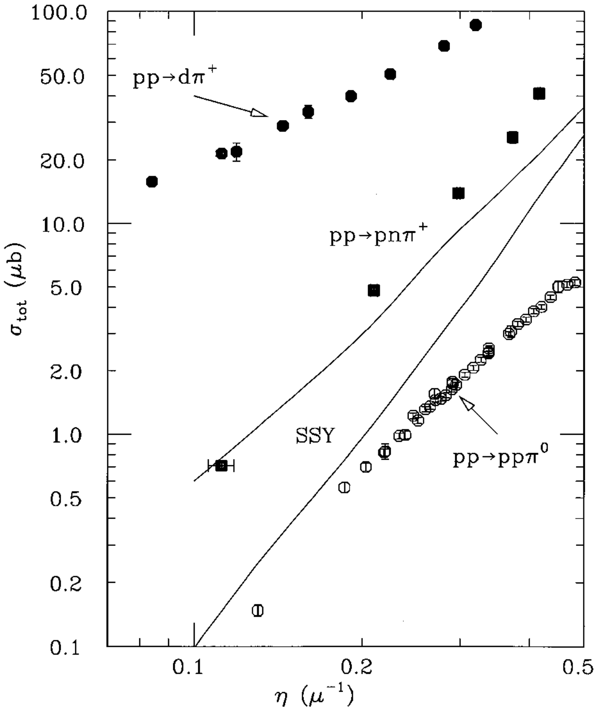

FIG. 17. Comparison of new data with calculations and related reactions. The new cross sections for the reaction $pp\to pn\pi^+$ are compared to $pp\to pp\pi^0$ data by Meyer *et al.* and $pp\to d\pi^+$ cross sections by Hutcheon *et al.* Near threshold the cross sections rise as monotonic, but differing functions of η. The solid lines show two theoretical prediction by Schillaci *et al.* for $pp\to pn\pi^+$. (The recent, relativistic one-boson exchange calculation of Engel *et al.* is not shown. It agrees with known cross sections in the 1–2 GeV region, but underpredicts the cross section near threshold.)

to threshold, requiring an additional component with η^3 dependence starting at $\eta\simeq0.14$. A distinct η dependence sometimes permits the separation of s- and p-wave πN components, but the $pp\to pn\pi^+$ s-wave phase space is expected to be a combination of several powers of η and the available data for $pp\to pn\pi^+$ do not permit a reliable separation.

We note that the $pp\to d\pi^+$ cross sections are more than an order of magnitude larger than those for the $pp\to pn\pi^+$ channel, which in turn are a factor of about 5 larger than the $pp\to pp\pi^0$ data. Their relative pion production strengths can be understood qualitatively. The $pp\to pp\pi^0$ reaction has total isospin 1 for the initial and final NN state. The reaction $pp\to pn\pi^+$ also has isospin 1 for the initial state but 1 and 0 for the final NN state. Isospin is a good quantum number in strong interactions [5], and the $pp\to pn\pi^+$ cross section must be larger since the amplitudes for different NN isospin add incoherently. Very close to threshold, both transitions should be dominated by s-wave final NN states. We expect dominant contributions of ${}^1S_0$ for $pp\to pp\pi^0$ and ${}^1S_0$ and ${}^3S_1$ for $pp\to pn\pi^+$, each of which can produce enhancements at low NN relative energy. Compared to $pp\to pn\pi^+$, the s-wave and p-wave pion rescattering amplitudes are greatly suppressed for $pp\to pp\pi^0$. Here s-wave suppression results from the accidental cancellation of πN scattering lengths and p-wave suppression comes from the absence of ΔN intermediate states of angular momentum zero for $pp\to pp\pi^0$.

The $pp\to pn\pi^+$ and $pp\to d\pi^+$ reactions differ in that the latter is restricted to a ${}^3S_1$ or ${}^3D_1$ pn state while in the former more scattering states are allowed; however, the very large total cross section for $pp\to d\pi^+$ has other causes. The relation of the ${}^3S_1$ strengths between $pp\to pn\pi^+$ and $pp\to d\pi^+$ total cross section has been explained by Lee [43] who found that the $pp\to d\pi^+$ cross section is larger because orthogonality requires the pn scattering state wave function to have a node whereas the pn bound state has none. This makes the overlap with the π wave function and the cross sections much smaller for $pp\to pn\pi^+$.

The earliest attempt to quantitatively correlate all three pion production channels was made in the early PCAC calculations of Schillacci, Silbar, and Young [7]. Because of the lack of information about the NN interaction and its off-shell behavior at the time this work was done, only a range of values could be predicted, as shown in Fig. 17. Close to threshold their respective ranges are in qualitative agreement with both the new $pp\to pn\pi^+$ and $pp\to pp\pi^0$ experimental cross sections and their energy dependence. There are discrepancies in detail. Their off-shell approximation gave the best agreement for $pp\to pn\pi^+$, but for $pp\to pp\pi^0$ their on-shell approximation (corresponding to the lower curve in Fig. 17) was closest to the data. A similar prediction for $pp\to d\pi^+$ failed, presumably because of an inadequate treatment of the deuteron wave function. This calculation could be done with less ambiguity today because the off-shell NN interaction is much better understood.

Other calculations published so far either specialize in describing the $pp\to d\pi^+$ or the $pp\to pp\pi^0$ reactions. The major difference between the $pp\to pp\pi^0$ calculations of Koltun and Reitan, Niskanen, and Miller and Sauer (all of which are too small by a factor of 5) and most of the calculations that exhibit agreement with the data [7,25,24,26] is the use of a more complete NN interaction in the pion rescattering terms. Horowitz *et al.* and Lee and Riska explicitly include the effect of higher mass mesons as in Fig. 1(c), whereas Schillacci, Silbar, and Young included the same physics in a more phenomenological way.

In order to avoid fortuitous agreement it seems important to simultaneously study related reactions where the various mechanisms will contribute differently. For example, Lee [43] finds that the isoscalar heavy meson exchange is dominant in $pp\to pp\pi^0$ but less important for $pp\to pn\pi^+$, where the rescattering diagram is the most important one. He gets a satisfactory description of the total cross sections for all three reactions in a calculation that extends the Lee and Riska model [24] to charged pion production. Lee finds that the pion rescattering diagram is much more significant for $pp\to pn\pi^+$ and $pp\to d\pi^+$ than for $pp\to pp\pi^0$. The contribution of the Δ resonance is not included in his calculation. Although the Δ is suppressed in $pp\to pp\pi^0$, it must be considered for $pp\to pn\pi^+$ and $pp\to d\pi^+$ to make a quantitative comparison. Further theoretical study of these issues is clearly needed.

Below, we will provide a more detailed description of the experimental results. In choosing variables to display, we were guided by the physical effects that are expected to be important as we investigate the πNN vertex. The pion angular distribution carries information about the contributing partial waves of the pion with respect to the pn pair. Next, the invariant mass distributions of the $n\pi^+$ and $p\pi^+$ pairs can be examined. A complete picture of the reaction also requires a description of the pn pair, both for determination of their properties and because their angular momentum state strongly affects the pion angular distribution. We will present a partial wave amplitude analysis and other evidence for dominance of s waves in both the pn and $\pi(pn)$ systems.

B. Invariant mass distributions and Dalitz plots

The structure of the final state pn pair can be observed through the distribution of their invariant mass M_{pn}. We find that, generally, the final state pn pair has very low relative energy in this reaction. When the pion has its maximum momentum, the recoiling nucleons must travel together with zero relative momentum and M_{pn} is just the sum of proton and neutron masses. The strong final state interactions in the $l=0$ partial waves will have a dominant role in this situation. At the highest beam energy for this experiment (319.2 MeV), the maximum allowed value of M_{pn} is 1890.31 MeV and the available relative kinetic energy for the pn pair in the c.m. frame ranges from 0 to 12.47 MeV. At the lowest beam energy, the available kinetic energy ranges from 0 to 0.92 MeV. These allowed ranges are very close to the ranges of pion energy in the c.m. frame because M_{pn} is at its minimum when $E_{\pi,\text{c.m.}}$ is at it maximum and vice versa. In fact, these variables are strongly correlated since

$$M_{pn}^2 = s + m_\pi^2 - 2E_{\pi,\text{c.m.}}\sqrt{s}, \tag{7}$$

where $\sqrt{s}$ is the total energy of the system in the c.m. Figure 18 shows the measured distributions of M_{pn} for two beam energies. The arrows show the kinematic limits. The experimental resolution in M_{pn} is less than the bin size in each case. There is a strong peaking for low M_{pn} as would be expected for an s-wave final state interaction. The distribution of M_{pn} events can be reproduced in a Monte Carlo calculation assuming a pn FSI of appropriate strength (see Sec. III D; a similar result is seen in the CELSIUS $pp \rightarrow pp\pi^0$ experiment [10]).

A general view of the three-body final state can be provided by a Dalitz plot. In Fig. 19 we plot the invariant mass of the pn pair against that of the πp pair for the highest beam energy. In the figure, the small M_{pn} and large $M_{\pi p}$ are strongly correlated, and so an increase in the yield at large $M_{\pi p}$ due to the onset of p waves cannot be distinguished from an enhancement at small M_{pn} due to final state interactions in this plot. However, we note that the mass distributions for $M_{\pi n}$ and $M_{\pi p}$ shown in Fig. 20 are very similar. This would only occur if the Δ was a minor contributor since the isospin Clebsch-Gordon coefficient for coupling to the Δ for $\pi^+ p$ is 3 times larger than for $\pi^+ n$. (The effect in the cross section will be a factor of 9.)

At present, there are no theoretical calculations available for any of these quantities. The observed invariant mass distributions present qualitative evidence for the dominance of pn s waves. There is strong peaking of M_{pn} where the pn relative momentum is close to zero. We were able to reproduce this M_{pn} event distribution in a Monte Carlo calculation using a realistic pn FSI. Although use of a p-wave πN interaction in the Monte Carlo calculation was also able to generate a peak at low M_{pn}, we were unable to reproduce the full M_{pn} distribution with reasonable parameters.

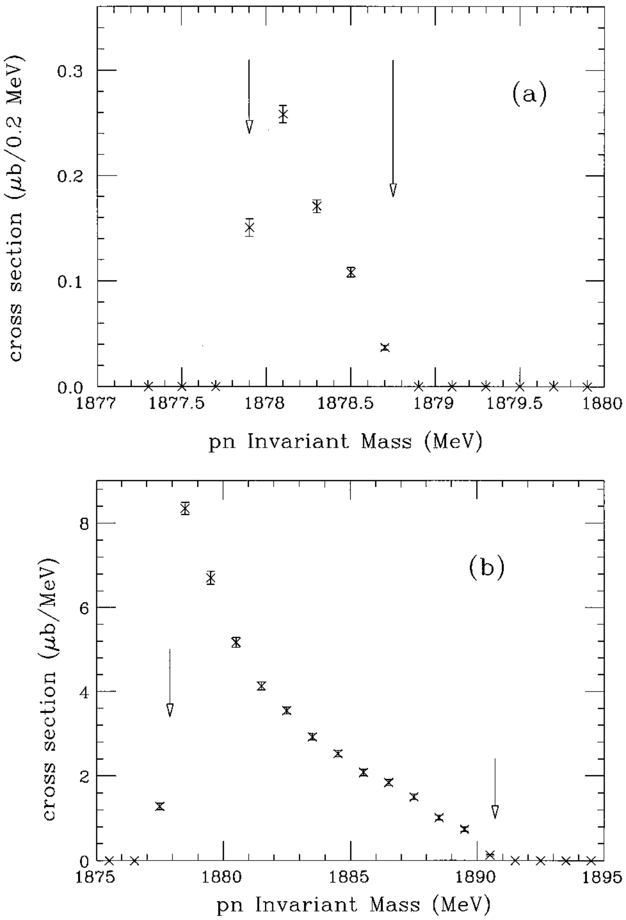

FIG. 18. Pion production cross sections as a function of pn invariant mass for (a) 294.3 and (b) 319.2 MeV beam energy, deduced without including final state interactions in the acceptance calculation. The kinematic end points are indicated by arrows. The strong peaking at low pn invariant mass suggests the presence of strong final state interactions.

In the next section, we present further and more quantitative evidence for the dominance of s waves based on the pion angular distributions.

C. Pion differential cross sections

Differential cross sections for pion production with respect to the pion angle in the c.m. frame at bombarding energies of 294.3, 299.3, and 319.2 MeV are plotted in Fig. 21 and listed in Table III. The errors shown include contributions from statistics and from estimated errors in the acceptance calculation. These contributions are roughly equal in size except for the lowest energy where uncertainties from energy and angle calibrations dominate. The errors in the c.m. pion angle are energy dependent because of the kinematic focusing close to threshold. Based on Monte Carlo calculations, we estimate pion angular resolutions of 19° at 294.3 MeV and 5° at 319.2 MeV.

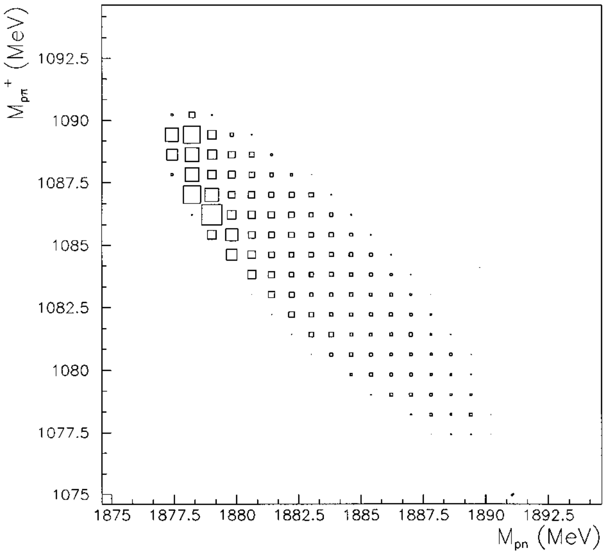

FIG. 19. The Dalitz plot for 319.2 MeV data with phase space acceptance not including FSI. These plots show the invariant mass of the proton-pion pair vs the invariant mass of the proton-neutron pair. All values in the kinematically allowed region are populated in this experiment to some degree. There is a strong enhancement at low M_{pn} and high M_{π^+p}. This would be expected from strong pn final state interactions.

The kinematically complete measurements permit us to calculate cross sections in any reference frame, but there are a number of advantages to the c.m. frame defined by the entrance channel. This is the frame that is commonly used for presenting $pp\rightarrow d\pi^+$ angular distributions, and so the interpretations are similar. As for $pp\rightarrow d\pi^+$, only even powers of $\cos\theta$ can contribute to the differential cross section. Symmetry in the angular distributions about 90° is expected but it was not imposed on the data. Data points at the same value of $\cos^2\theta$ are observed to differ by less than one standard deviation, giving independent support for the validity of the analysis.

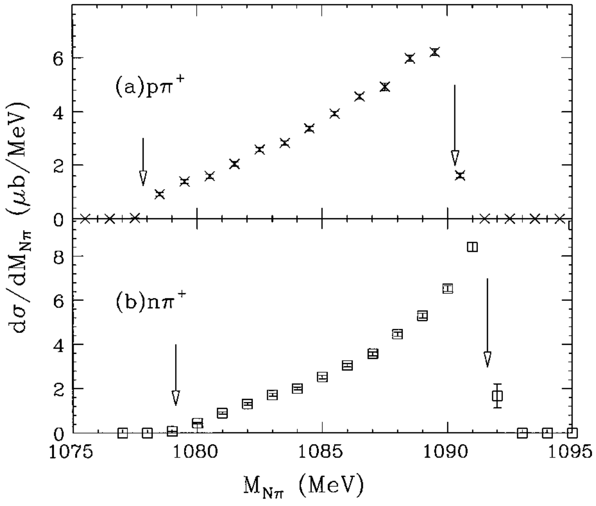

FIG. 20. Invariant mass of the (a) proton plus pion and (b) the neutron plus pion system at 319.2 MeV beam energy. These distributions were determined using an acceptance calculation that included the FSI effects discussed in the text. The similarity of these two distributions is an indication that the Δ resonance is not a major contributor to the $pp\rightarrow pn\pi^+$ reaction in this energy range since the π^+p amplitude couples to the Δ three times more strongly than the π^+n amplitude.

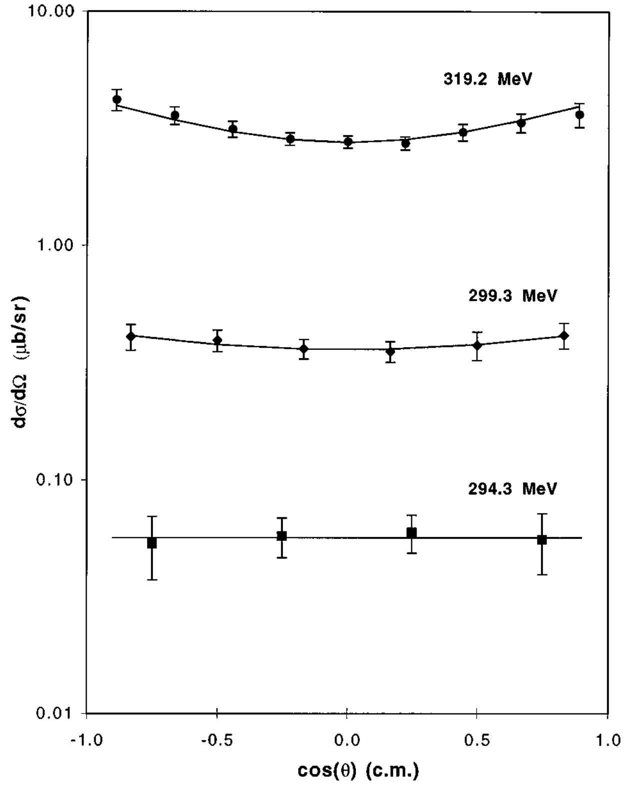

FIG. 21. Pion angular distributions in the three-body center-of-mass frame labeled by laboratory beam energy (294.3 MeV, 299.3 MeV, and 319.2 MeV). The solid lines are fits using the equation $d\sigma/d\Omega = A + BP_2(\cos\theta)$, which measures the anisotropy of the distribution. The 294.3 MeV and 299.3 MeV error bars are dominated by angle-dependent systematic errors arising from energy calibration uncertainties (see Fig. 15). Only the data at 319.2 MeV show a significant anisotropy.

Within errors, the pion angular distributions are isotropic close to threshold. Isotropy indicates either s-wave πNN mechanisms or an unusual combination of p-wave mechanisms. To determine the s-wave πN strength, a partial wave amplitude analysis must be applied to these angular distributions. Such an analysis was discussed in some detail for $pp\rightarrow d\pi^+$ [12,44]. The typical ordering for three-body final states labels the NN pair and the pion relative to the NN pair [5,6]. The situation is more complicated for three-body final states because the final state NN pair can be in a variety of angular momentum states. If the orbital angular momentum of the NN pair is 0 and the pion is restricted to $L_\pi = 0$ or 1, there is only one contributing s-wave amplitude for $pp\rightarrow pp\pi^0$. There are three such amplitudes for $pp\rightarrow d\pi^+$ and four for $pp\rightarrow pn\pi^+$. If one also allows $L_{NN}=1$, the total number of amplitudes increases to 3, 12, and 19, respectively.

TABLE IV. Partial wave amplitudes that can contribute to $pp \rightarrow pn\pi^+$ and involve only $L=0$ for the final state nucleons. The first column gives the amplitude name [44,46] used for the quantum states listed in the second, third, and fourth columns for the initial NN states, final NN states, and the $\pi(NN)$ states, respectively. An × in the last two columns denotes the other pion production channels where these amplitudes can contribute.

Label	NN initial state	NN final state	$L_{\pi(NN)}$	$pp \rightarrow d\pi^+$	$pp \rightarrow pp\pi^0$
a_0	$^1S_0$	$^3S_1$	1	×	
a_1	$^3P_1$	$^3S_1$	0	×	
a_2	$^1D_2$	$^3S_1$	1	×	
b_0	$^3P_0$	$^1S_0$	0		×

For the $L_{NN}=0$ final states (see Sec. IV B), the relevant amplitudes for each of the pp inelastic reactions are listed in Table IV. Since $pp \rightarrow pn\pi^+$ and $pp \rightarrow pp\pi^0$ are related by isospin, the same $b_0(\eta)$ values should apply to both reactions. However, $pp \rightarrow pn\pi^+$ and $pp \rightarrow d\pi^+$ have the pn pair in unbound and bound states, respectively, and so there is little reason to expect that the partial wave amplitudes will be the same in these reactions. Nevertheless, we anticipate the same qualitative behavior for $pp \rightarrow d\pi^+$ and $pp \rightarrow pn\pi^+$ for issues involving spin couplings. In the analysis of $pp \rightarrow d\pi^+$ by Korkmaz *et al.* [12], the principal s-wave πN amplitude is a_1 which gives an isotropic differential cross section for both $pp \rightarrow pn\pi^+$ and $pp \rightarrow d\pi^+$, and the principal p-wave πN amplitude is a_2 which leads to a cross section proportional to $1+3\cos^2\theta$. The amplitude a_2 is expected to be significant for both $pp \rightarrow pn\pi^+$ and $pp \rightarrow d\pi^+$ because the intermediate $N\Delta$ state can be in a relative s wave. As with a_2, the a_0 amplitude has $L_\pi=1$, but if the mechanism goes through an $N\Delta$ intermediate state, the $N\Delta$ pair must be coupled to $L=2$ [12], which is less likely near threshold for both $pp \rightarrow pn\pi^+$ and $pp \rightarrow d\pi^+$. The other s-wave πN amplitude in Table IV is b_0 which is the primary contributor to $pp \rightarrow pp\pi^0$. Since the $pp \rightarrow pp\pi^0$ total cross section is a factor of $\simeq 5$ lower than that of $pp \rightarrow pn\pi^+$, b_0 should be less significant than the other s-wave parameters for $pp \rightarrow pn\pi^+$.

The angular distributions for the three reactions (considering only the $L_{NN}=0$ final state) were derived from the formalism introduced by Mandl and Regge [45]:

$$pp \rightarrow d\pi^+,$$

$$\frac{d\sigma}{d\Omega}=\frac{1}{4}(|a_0'|^2+|a_1'|^2+|a_2'|^2)+\left(\frac{1}{4}|a_2'|^2-\sqrt{\frac{1}{2}}\mathrm{Re}[a_0'a_2'^*]\right)P_2(\cos\theta), \qquad (8)$$

$$pp \rightarrow pp\pi^0, \quad \frac{d\sigma}{d\Omega}=\frac{|b_0|^2}{12}, \qquad (9)$$

TABLE V. Parameters for the observed $pp \rightarrow pn\pi^+$ angular distributions fit using the form $d\sigma/d\Omega=A+BP_2(\cos\theta)$.

Beam energy (MeV)	A (μb/sr)	B (μb/sr)
294.3	0.057 ± 0.006	0.000 ± 0.014
299.3	0.38 ± 0.02	0.048 ± 0.045
319.2	3.27 ± 0.10	1.02 ± 0.24

$$pp \rightarrow pn\pi^+,$$

$$\frac{d\sigma}{d\Omega}=\frac{1}{4}\left(|a_0|^2+\frac{1}{3}|b_0|^2+|a_1|^2+|a_2|^2\right)+\left(\frac{1}{4}|a_2|^2-\sqrt{\frac{1}{2}}\mathrm{Re}[a_0a_2^*]\right)P_2(\cos\theta), \qquad (10)$$

where P_2 is a Legendre polynomial. The equations are similar to those given in other treatments of these reactions. [44,46,12] Although the matrix elements a_ν and a_ν' refer to the same quantum numbers, they should differ in value because the total cross sections are quite different in magnitude (as discussed above). The analysis of Korkmaz *et al.* for $pp \rightarrow d\pi^+$ found a_0 consistent with zero and $|a_2| \simeq 2.5|a_1|\eta$ for values of η very similar to those in this experiment. The large ratio was required to simultaneously fit the angular distributions and the strong analyzing powers seen in their data.

The smooth and nearly isotropic angular distributions seen in our experiment suggest that only a small number of amplitudes is likely to contribute and that s waves are more important in $pp \rightarrow pn\pi^+$ than for $pp \rightarrow d\pi^+$. We fit the differential cross sections to the relation $d\sigma/d\Omega=A+BP_2(\cos\theta)$ and list the strengths A and B in Table V. Although our differential cross sections alone do not permit us to deduce all four amplitudes of Table IV or Eq. (10), a tentative result can be obtained by utilizing existing information for b_0 and a_0'. It is reasonable to assume that the $pp \rightarrow pp\pi^0$ data [9,10] are dominated by the s-wave amplitude and therefore determine b_0^2. In addition, a_0' was shown to be very small by Korkmaz *et al.* [12] for $pp \rightarrow d\pi^+$, and in order to be able to deduce $|a_1|^2$ and $|a_2|^2$ we assume that similarly $a_0 \approx 0$. Using Eqs. (9) and (10), tentative values for $|a_1|^2$ and $|a_2|^2$ were extracted at three values of η and are shown in Fig. 22. We note that the ratio of $|a_2|^2$ to $|a_1|^2$ is much larger for $pp \rightarrow d\pi^+$ than for $pp \rightarrow pn\pi^+$. Simple arguments [6] predict an energy dependence proportional to η^2 for $|a_1|^2$ and proportional to η^4 for $|a_2|^2$. The lines in Fig. 22 illustrate that partial cross sections are compatible with simple power law dependences, requiring an exponent of 2.8 for $|a_1|^2$ and about 5.2 for $|a_2|^2$. These qualitatively different powers suggest that the originally proposed simple power relations like 2 and 4 [6] are derived from inadequate models.

A theoretical extrapolation of $pp \rightarrow pn\pi^+$ cross sections from known $pp \rightarrow pp\pi^0$, and $pp \rightarrow d\pi^+$ data by Faeldt

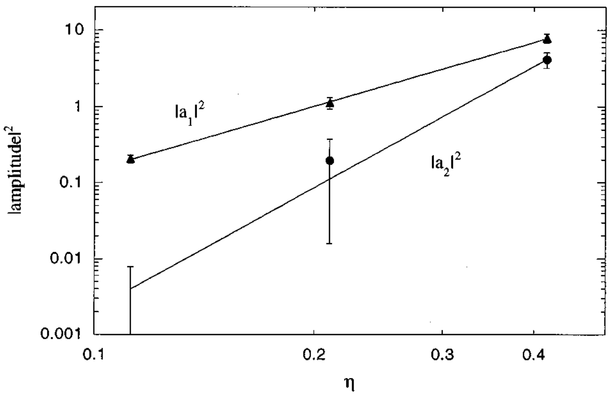

FIG. 22. Tentative energy dependence of the partial wave amplitudes $|a_1|^2$ (triangles) and $|a_2|^2$ (solid circles) for $pp \rightarrow pn\pi^+$, in units of μb/sr. Uncertainties due to random errors and angle-dependent systematic errors are shown. All cross sections also have a common ±15% scale error, which is not shown. The solid lines show fits to the points assuming a power relationship $|ME|^2 = \eta^\alpha$, where $\alpha =$ 2.8 and 5.2, respectively, are the fitted quantities.

and Wilkin obtains reasonable agreement with the observed $pp \rightarrow pn\pi^+$ energy dependence [47]. Recent refinements of their procedure also produce good agreement with the shape of the observed angular distribution, thus emphasizing the close relation between these reactions. A recent preprint by Shyam and Mosel uses a refined formalism of Ref. [16] to obtain similar, good agreement with the energy dependence and quite reasonable agreement with the angular distributions. It is of interest to see if their relativistic formalism is necessary. Both calculations obtain absolute cross sections within a range of about ±25% from the data.

V. SUMMARY AND CONCLUSIONS

We have presented kinematically complete data for the reaction $pp \rightarrow pn\pi^+$ near threshold. A novel experimental technique was discussed in some detail. The lowest proton beam energy for which cross sections are presented is 2.0 MeV over threshold where the *maximum* pion energy in the center-of-mass frame is 0.86 MeV ($\eta = 0.112$). With this experiment there now exist recent data for all three pp inelastic channels. This should facilitate reaching the long-term goal of extracting a model independent πNN vertex range in a reaction that necessarily requires πN off-shell scattering.

We observe that calculations using a soft pion theorem [7] are in qualitative (but so far not quantitative) agreement with the total cross sections of this experiment and for $pp \rightarrow pp\pi^0$. However, these calculations could be significantly improved using modern inputs, particularly the NN off-shell interaction. With the exception of the calculation of Engel *et al.* [16], none of the recent calculations applied to $pp \rightarrow pp\pi^0$ have been published for $pp \rightarrow pn\pi^+$ at this time. Chiral perturbation theory has been applied to the $pp \rightarrow pp\pi^0$ reaction yielding a surprisingly poor description of the data [28,29]. However, the pion rescattering process is the main phenomenon that these calculations seek to describe; therefore, they should be more relevant for $pp \rightarrow pn\pi^+$ based on the arguments presented here. Calculations for $pp \rightarrow pn\pi^+$ would provide a better test of the range of applicability of chiral perturbation theory.

The relationship between the $pp \rightarrow pn\pi^+$ data and other pp inelastic channels close to threshold was discussed in terms of the amplitudes given in Table IV. The total cross sections for $pp \rightarrow d\pi^+$ near threshold are over an order of magnitude larger than that for $pp \rightarrow pn\pi^+$, which in turn is a factor of 5 larger than for $pp \rightarrow pp\pi^0$. These very different relative strengths are explainable through the use of realistic NN final state wave functions [43,47]. Lee also concluded that the $pp \rightarrow pn\pi^+$ cross sections are very sensitive to the off-shell πNN range. The interpretation of the $pp \rightarrow pp\pi^0$ data is still in dispute, as possibilities of large πN off-shell interaction strength and heavy meson exchange are being explored. A careful analysis of all pion production channels at threshold will be required for a consistent interpretation.

The invariant mass and angular distributions observed in $pp \rightarrow pn\pi^+$ indicate that close to threshold, s-wave angular momentum states dominate. The close similarity between the shapes of the invariant mass distributions for $n\pi^+$ and $p\pi^+$ gives evidence that the peaks in the pn invariant mass spectra are due to the s-wave pn interaction. Any theoretical calculation must include this pn final state interaction in order to correctly describe these data. The pion angular distributions closest to threshold are isotropic within errors; significant anisotropy of $pp \rightarrow pn\pi^+$ was observed only at 319.2 MeV. The anisotropy in each case is much smaller than that observed in $pp \rightarrow d\pi^+$ at the same η. Thus, the major conclusion at present is that these data are dominated by the amplitude a_1, which describes the pn and $\pi(pn)$ states as s-wave relative angular momentum states. Tentative values for the magnitude of a_1 are given for 294.3, 299.3, and 319.2 MeV. These data in conjunction with other recent near-threshold experiments should provide important new information about the πNN vertex.

ACKNOWLEDGMENTS

We would like to thank the staff of IUCF for their work in providing a clean, stable beam for this experiment, and K. Solberg, A. Eads, and G. Jacobs for technical help with the wire chambers. Thanks are due to D. Tedeschi and J. Williams for reanalyzing the luminosity data. We would also like to thank H.O. Meyer, T.-S.H. Lee, and F. Tabakin for useful and informative discussions. This work was supported through a medium energy grant by the National Science Foundation.

[1] S. L. Adler and R. F. Dashen, *Current Algebras and their Application to Particle Physics* (Benjamin, New York, 1968).

[2] J. Gasser and H. Leutwyler, Phys. Rep. **87**, 77 (1982).

[3] V. Bernard, N. Kaiser, and U. G. Meissner, Nucl. Phys. **B383**, 442 (1992).

[4] R. Beck, F. Kalleicher, B. Schoch, J. Vogt, G. Koch, H. Stroeher, V. Metag, J. C. McGeorge, J. D. Kellie, and S. J. Hall, Phys. Rev. Lett. **65**, 1841 (1990).

[5] M. Gell-Mann and K. M. Watson, Annu. Rev. Nucl. Sci. **4**, 219 (1954).

[6] A. H. Rosenfeld, Phys. Rev. **96**, 130 (1954).

[7] M. E. Schillaci, R. R. Silbar, and J. E. Young, Phys. Rev. **179**, 1539 (1969).

[8] S. L. Adler and Y. Dothan, Phys. Rev. **151**, 139 (1954).

[9] H. O. Meyer *et al.*, Phys. Rev. Lett. **65**, 2846 (1990); H. O. Meyer, C. Horowitz, H. Nann, P. V. Pancella, S. F. Pate, R. E. Pollock, B. Von Przewoski, T. Rinckel, M. A. Ross, and F. Sperisen, Nucl. Phys. **A539**, 633 (1992).

[10] A. Bondar *et al.*, Phys. Lett. B **356**, 8 (1995).

[11] S. Stanislaus, D. Horvath, D. F. Measday, A. J. Noble, M. Salomon, Phys. Rev. C **41**, 1913 (1990).

[12] E. Korkmaz, Jin Li, D. A. Hutcheon, R. Abegg, J. B. Elliot, L. G. Greenhaus, D. J. Mack, C. A. Miller, and N. L. Rodning, Nucl. Phys. **A535**, 636 (1991).

[13] D. A. Hutcheon *et al.*, Nucl. Phys. **A535**, 618 (1991). After completion of the manuscript two direct measurements of $pp \rightarrow d\pi^+$ appeared in print: M. Drochner *et al.*, Phys. Rev. Lett. **77**, 454 (1996), and P. Heimberg *et al.*, *ibid.* **77**, 1012 (1996).

[14] W. W. Daehnick, S. A. Dytman, J. G. Hardie, W. K. Brooks, R. W. Flammang, L. Bland, W. W. Jacobs, T. Rinckel, P. V. Pancella, J. D. Brown, and E. Jacobson, Phys. Rev. Lett. **74**, 2913 (1995).

[15] T.-S. H. Lee and A. Matsuyama, Phys. Rev. C **36**, 1459 (1987); T.-S. H. Lee (private communication).

[16] A. Engel, R. Shyam, U. Mosel, and A. K. Dutt-Mazumder, Nucl. Phys. **A603**, 387 (1996). See also R. Shyam and U. Mosel, LANL Report No. nucl-th/9611013.

[17] J. T. Londergan, K. W. McVoy, and E. J. Moniz, Ann. Phys. (N.Y.) **86**, 147 (1974).

[18] B. C. Pearce and B. K. Jennings, Nucl. Phys. **A528**, 655 (1991).

[19] R. Machleidt, K. Holinde, and Ch. Elster, Phys. Rep. **149**, 1 (1987).

[20] V. G. J. Stoks, R. A. M. Klop, C. P. F. Terhagen, and J. J. deSwart, Phys. Rev. C **49**, 2950 (1994).

[21] J. Vogelzang, B. Bakker, and H. J. Boersma, Nucl. Phys. **A452**, 644 (1986).

[22] D. S. Koltun and A. Reitan, Phys. Rev. **141**, 1413 (1966).

[23] G. A. Miller and P. U. Sauer, Phys. Rev. C **44**, R1725 (1991).

[24] T.-S. H. Lee and D. O. Riska, Phys. Rev. Lett. **70**, 2237 (1993).

[25] C. Horowitz, H. O. Meyer, and D. Griegel, Phys. Rev. C **49**, 1337 (1993).

[26] E. Hernandez and E. Oset, Phys. Lett. B **350**, 158 (1995).

[27] C. Hanhart, J. Haidenbauer, A. Reuber, C. Schütz, and J. Speth, Phys. Lett. B **358**, 21 (1995).

[28] B.-Y. Park, F. Myhrer, J. R. Morones, T. Meisner, and K. Kubodera, Phys. Rev. C **53**, 1519 (1996).

[29] T. Cohen, J. Friar, G. Miller, and U. van Kolck, Phys. Rev. C **53**, 2661 (1996).

[30] C. Waltham *et al.*, Nucl. Phys. **A433**, 649 (1985).

[31] J. Hardie, Ph.D. thesis, University of Pittsburgh, 1993.

[32] P. Pile, in ''Proceedings of the Third LAMPF II Workshop,'' Los Alamos, NM, 1983, Report No. LA-9933-C (unpublished), Vol. II, p. 875.

[33] The lack of corrections for differential trigger efficiency and drift chamber edge effects for the analysis in our 1995 $pp \rightarrow pn\pi^+$ Letter distorted the ratio of elastic protons to reaction protons and, therefore, the absolute normalizations. The resulting errors were generally within the stated uncertainties except for 294 MeV where a 25% correction has been found.

[34] W. W. Daehnick, W. K. Brooks, S. Saha, and D. Kreithen, Nucl. Instrum. Methods Phys. Res. A **320**, 290 (1992).

[35] R. Arndt, I. Strakovsky, and R. Workman, Phys. Rev. C **50**, 731 (1994).

[36] R. Cecil, B. Anderson, and R. Madey, Nucl. Instrum. Methods **161**, 439 (1979).

[37] H. O. Meyer (private communication); M.A. Ross, Ph.D. thesis, Indiana University, 1991.

[38] K. M. Watson, Phys. Rev. **88**, 1163 (1952).

[39] A. Migdal, Sov. Phys. JETP **1**, 2 (1955).

[40] B. Morton, E. E. Gross, E. V. Hungerford, J. J. Malanify, and A. Zucker, Phys. Rev. **169**, 825 (1968).

[41] Physics Data: N-N Scattering Data, edited by J. Bystricky and F. Lehar, Report No. 11-2, 1981.

[42] B. J. Ver West and R. A. Arndt, Phys. Rev. C **25**, 1979 (1982).

[43] T.-S. H. Lee, LANL Report No. nucl-th/9502005.

[44] B. Blankleider and I. R. Afnan, Phys. Rev. C **31**, 1380 (1985).

[45] F. Mandl and T. Regge, Phys. Rev. **99**, 1478 (1955).

[46] B. Blankleider, in *Particle Production near Threshold*, edited by E. Stephenson and H. Nann, AIP Conf. Proc. No. 221 (AIP, New York, 1991), p. 150.

[47] G. Faeldt and C. Wilkin, Phys. Lett. B **382**, 209 (1996); and (private communication).